The role of cohesin loading at enhancers in the flux of loop extrusion and long-range transcriptional control

Erika C. Anderson[1], Hadi Rahmaninejad[2], Abrar Aljahani[3], Emily M. Arnold[1], Annie S. Adachi[1], Rini Shah[1], Karissa L. Hansen[1], Ivana Cavka[3], Alistair N. Boettiger[3], Geoffrey Fudenberg[2], Elphège P. Nora[1,4,5,*]

1. Cardiovascular Research Institute, University of California, San Francisco, San Francisco, CA, USA
2. Department of Quantitative and Computational Biology, University of Southern California, Los Angeles, CA, USA
3. Department of Developmental Biology, Stanford University; Stanford, CA 94305, USA
4. Department of Biochemistry and Biophysics, University of California, San Francisco, San Francisco, CA, USA
5. Chan-Zuckerberg Biohub San Francisco, CA, USA
*correspondence: elphege.nora@ucsf.edu

Abstract

Enhancers have been proposed to act as privileged loading sites for cohesin, raising the idea that they actively fold the genome to engage distal target promoters for transcription. Supporting this idea, NIPBL/MAU2, which is required for cohesin loading, binds at enhancers in mouse embryonic stem cells. However, we find that driving cohesin recruitment near an enhancer strongly inhibits transcription from its target distal promoter, indicating that strong focal cohesin loading at enhancers is not compatible with their long-range regulatory functions. Quantitative experiments and biophysical modeling further indicate that cohesin loading at enhancers does not make major contributions to genome-wide cohesin binding and chromosome folding patterns. Instead, cohesin must load throughout the genome to extrude it, regardless of enhancer proximity, with the major determinants of cohesin traffic being extrusion barriers such as transcription and clustered CTCF sites. These findings indicate that enhancer function is largely ancillary to the general mechanisms of chromosome folding, informing further study of the relationship between genome architecture and transcriptional regulation.

Main Text

Introduction

Enhancers are genetic elements able to modulate the activity of target promoters over long genomic distances. Such regulatory communication is supported by chromatin loops that bring distal loci into physical proximity within the cell nucleus[1,2]. The cohesin complex plays a key role in this process by dynamically extruding chromatin loops[3,4]. Yet, how the flux of cohesin loop extrusion is controlled to support long-range enhancer-promoter communication remains unclear.

Several studies have proposed that enhancers themselves may serve as loading sites for cohesin[5–12], thereby directly initiating chromatin loops to contact distal promoters (Fig. 1A). In this view, enhancer function would extend to the reshaping of chromosome folding in ways that support the delivery of their regulatory activity to distal promoters.

Support for targeted cohesin loading at enhancers initially came from the observation that, in mammalian genomes, cohesin binds distal regulatory elements along with NIPBL/MAU2[10,13–18]. NIPBL/MAU2 was originally defined as the cohesin loader complex, as it is required to initiate (but not maintain) topological cohesin binding during sister chromatid cohesion[19,20]. In the context of loop extrusion, NIPBL/MAU2 is required for both initiation and extension of extrusion[21–24]. The presence of NIPBL/MAU2 has therefore been interpreted as an indication of cohesin loading and looping from enhancers[10,13,15]. This interpretation was reinforced by the observations that enhancers can locally increase cohesin occupancy[8,11] and create characteristic chromosome folding signatures such as Hi-C jets/fountains and stripes across organisms[10,25–30].

However, for loading at enhancers to support long-range looping with distal promoters, cohesin would need to remain stably anchored at the enhancer during extrusion; otherwise cohesin would extrude away from the enhancer before reaching the target promoter (Fig. 1A). Yet, evidence for systematic anchoring of cohesin at enhancers is lacking.

At the same time, alternative models have suggested that cohesin loading is not restricted to discrete NIPBL/MAU2 binding sites (Fig. 1A), but may instead occur in a largely uniform fashion across the genome. Indeed, quantitative simulations of chromosome folding better fit Hi-C and imaging results (including stripes) when they assume uniform rather than targeted cohesin loading[31–33]. Furthermore, many enhancers regulate promoters several hundreds of kilobases away[34–36], at distances that greatly exceed the average processivity of cohesin molecules that would load at enhancers. Such distances could be bridged by multiple cohesins that load at different loci, but not by exclusive loading at the enhancer. Finally, cohesin loading cannot simply be restricted to topologically associating domains (TADs) containing enhancers, as constitutive heterochromatin is also extruded[37].

Together, these considerations raise the question to what extent enhancers actively shape chromatin interactions by acting as the loading sites for extrusive cohesin, versus simply operating within the ongoing flux of cohesin extrusion. Despite the relevance to our understanding of the coupling between transcriptional regulation and chromosome folding, discriminating between these possibilities has proven challenging, as it requires interpreting steady-state measurements of cohesin binding and Hi-C within mechanistic models of extrusion dynamics.

Here, we investigate the idea that long-range transcriptional regulation in mammalian cells is facilitated by loading of extrusive cohesin at enhancers through the recruitment of NIPBL/MAU2. We find that, while transcription factors can recruit NIPBL/MAU2 to enhancers, most cohesin molecules load outside enhancers. Artificially recruiting MAU2 to increase cohesin loading and looping near enhancers fails to support distal promoter activation and is instead detrimental to transcription, indicating that highly targeted cohesin loading is incompatible with long-range regulation by enhancers. Consistent with this, genome-wide analyses and quantitative biophysical simulations show that targeted loading at enhancers contributes little, if at all, to the general flux of cohesin extrusion across chromosomes. Instead, cohesin positioning genome-wide is best explained by pervasive loading combined with blocking by transcription and clustered CTCF sites. Together, these results indicate that enhancers do not initiate cohesin loops to support their own action in long-range transcriptional control, and that instead their regulatory opportunities are largely subordinate to the global dynamics of cohesin loop extrusion.

Results

Transcription factors recruit NIPBL/MAU2 at enhancers without substantially enriching cohesin

Enhancers have initially been proposed to act as loading sites for extrusive cohesin because they can bind NIPBL/MAU2[10,15]. Given the reported technical difficulties with NIPBL ChIP-seq[31,38], we first sought to identify high-confidence NIPBL and MAU2 binding sites. We performed spike-in calibrated ChIP-seq with an HA antibody in mouse embryonic stem cells (ESCs) with either endogenous NIPBL or MAU2 tagged with both an HA epitope tag and a dTAG-inducible degron and identified ~24,000 binding sites (Extended Data Fig. 1A-B). These binding sites were absent in cells where NIPBL or MAU2 was degraded and in cells without an HA tag, ruling out any false positives resulting from antibody binding nonspecifically or to hyper-ChIPable open chromatin (Extended Data Fig. 1B). As expected, HA-NIPBL and HA-MAU2 binding closely matched each other (Extended Data Fig. 1B), and ChIP-seq with an antibody for endogenous NIPBL showed binding at these same sites (Extended Data Fig. 1C). Although these NIPBL and MAU2 ChIP peaks are reproducible, the ChIP signal (with multiple different antibodies) displayed much lower enrichment above background compared to ChIP for other factors (Extended Data Fig. 1G-H). This low enrichment suggests that a substantial amount of the NIPBL/MAU2 molecules bind – and possibly function – outside the peaks.

We analyzed the genomic locations of NIPBL/MAU2 binding, and found that NIPBL/MAU2 was enriched at predicted enhancers (defined as sites bound by the pluripotency transcription factors OCT4, SOX2, and NANOG[39]). In contrast, binding was much less pronounced at active transcription start sites, which show high enrichment for H3K27ac but not pluripotency transcription factors (Fig. 1B-C, Extended Data Fig. 1D-E). Therefore, NIPBL/MAU2 does not simply bind all active chromatin but tracks the binding of pluripotency transcription factors.

To further explore the specificity of NIPBL/MAU2 binding at enhancers, we tested whether transcription factor binding is sufficient to recruit NIPBL/MAU2 and load cohesin (Fig. 1D). We used human U2OS cells with a microscopically visible TetO array spanning ~4 Mb[40], a recruitment platform large enough for loaded cohesin to not simply extrude away. Tethering OCT4 and VP64 to the TetO array was sufficient to recruit endogenous NIPBL and MAU2 (Fig.

1E-F, Extended Data Fig. 2) indicating that the ChIP-seq enrichment of NIPBL/MAU2 at enhancers in ESCs is indeed due to recruitment by transcription factors (directly or indirectly via transcriptional cofactors), and that NIPBL/MAU2 recruitment is not limited to pluripotency factors.

Cohesin did not, however, localize to the TetO array upon OCT4 or VP64 recruitment, despite the presence of NIPBL/MAU2. The lack of detectable cohesin upon transcription factor tethering suggests that NIPBL/MAU2 binding to active regulatory elements is not necessarily molecularly coupled to local cohesin recruitment. The low amount of NIPBL/MAU2 recruited by transcription factors is therefore insufficient to cause detectable cohesin accumulation, or NIPBL/MAU2 is not readily competent for loading cohesin when recruited by transcription factors. Recruiting larger amounts of MAU2 by direct fusion to TetR visibly enriched cohesin (Fig. 1E, Extended Data Fig. 2A-B) – demonstrating that upon sufficient loading, cohesin is readily detected by this assay.

Very strong cohesin loading sites are incompatible with regulation by enhancers

After confirming that NIPBL/MAU2 binds enhancers, we next tested the model that focal cohesin loading at enhancers increases interactions with distal promoters and benefits long-range transcriptional activation. We used the TACL system[41] to force cohesin loading at the *Car2* locus in ESCs (Fig. 2A), which depends on cohesin for transcriptional activation by distal enhancers[42]. In a cell line where one *Car2* allele encodes a GFP reporter while the other allele encodes RFP (Extended data Fig. 3A), we heterozygously inserted a TetO array either beside the promoter, between the promoter and enhancers, or beside the enhancers, and expressed TetR-MAU2 to target cohesin loading at the TetO array (Fig. 2B). In contrast to the expectation that increasing cohesin loading would bolster activation by the distal enhancers, we observed strong downregulation of *Car2* upon forcing cohesin loading from any of the three TetO locations (Fig. 2B, Extended Data Fig. 3B). Reporter expression was unaffected by TetR alone binding to the TetO array, and expression of the *Car2* reporter on the control allele without a TetO insertion was unchanged (Extended Data Fig. 3C), ruling out possible indirect effects of MAU2 overexpression. Thus, despite the dependence of *Car2* expression on loop extrusion[42], strong cohesin loading at the enhancer impairs transcriptional activity.

To gain insight into the changes in chromatin folding caused by targeted cohesin loading, we used optical reconstruction of chromosome architecture (ORCA, Fig. 2C), which allowed us to specifically probe the *Car2* allele harboring the TetO array (Extended Data Fig. 4A, Methods). Targeting cohesin loading either beside the enhancers or beside the promoter did not increase enhancer-promoter interactions, which remained largely unaffected (Fig. 2D-E, Extended Data Fig. 4C-E). Targeting loading between the enhancers and the promoter separated them by creating a boundary that slightly reduced their interactions (Fig. 2D-E). Therefore, targeted loading-induced transcriptional repression, which occurs from all three configurations, cannot be simply explained by a change in enhancer-promoter interactions. Rather, high levels of extruding cohesin appear to repress transcription by disrupting enhancer or promoter activity, possibly by interfering with assembly or progression of the transcription machinery. Since strong cohesin loading at enhancers is detrimental to transcription from distal promoters, it is unlikely that enhancers generally serve as strong loading sites.

Polymer simulations show that focal cohesin loading can only moderately impact cohesin traffic

Given our observation that high targeted cohesin loading compromises enhancer function, we sought to establish how more modest loading at NIPBL/MAU2 sites would influence cohesin traffic and chromosome folding. As cohesin at NIPBL/MAU2 sites has been interpreted as a signature of targeted loading[10,43], we first used biophysical simulations[44] to explore how much cohesin binding is expected at loading sites across a range of loading rates (Fig. 3A). Using extrusion parameters selected to match measurements in mouse ESCs (Methods), we simulated a uniform background loading rate with elevated loading at a target site and found that bidirectionally extruding cohesin would not accumulate at loading sites, even with up to a 500-fold boost in on-target loading over the background loading rate (Fig. 3B). Instead, cohesin rapidly extrudes away from the loading site.

We next explored to what extent loading sites are expected to increase cohesin accumulation at nearby CTCF sites. To address this, we added to the simulations two dynamic barriers[45] flanking the loading site at varying distances (Fig. 3C). The simulations revealed that although targeted loading can, in principle, influence cohesin traffic, the impact remains limited. Even for CTCF barriers only 5 kb from the loading site, increasing cohesin accumulation two-fold would require more than a 500-fold boost in on-target loading rate (Fig. 3D). The reason focal loading has limited impact is that the amount of cohesin contributed by targeted loading sites is overshadowed by the cohesins loaded elsewhere along the chromosome. For example, with on-target loading increased 500-fold, a 250 bp loading site would contribute a similar amount of cohesin as background loading from the 125 kb of surrounding chromatin, thereby only increasing cohesin accumulation at the CTCF barrier ~two-fold. Thus, cohesin traffic to nearby barriers is expected to be dominated by chromosome-wide loading rather than by even strongly privileged loading sites.

Finally, we explored the signatures of targeted cohesin loading on Hi-C patterns. 3D polymer models indicated that high focal loading causes the emergence of fountain patterns in contact maps (Extended Data Fig. 5A-B), as observed in previous simulations [25,26]. Yet, these patterns do not increase the interactions of the loading site with its surrounding genomic environment (Extended Data Fig. 5A-B, Supplementary video), as cohesin extrudes away from the loading site. We observed that, at high loading rates, wider multi-kilobase loading sites create a boundary with stripes on contact maps (Extended Data Fig. 5B), due to multiple closely loaded cohesins colliding with each other. Although such a boundary at a large loading site could anchor cohesin, our TACL results indicate that such a configuration impairs long-range transcriptional regulation (Fig. 2).

Most cohesin resides outside CTCF sites

Having defined expectations of how targeted loading can influence cohesin positioning, we next quantified cohesin localization in ESCs to determine the extent to which NIPBL/MAU2 sites at enhancers contribute to initiating loop extrusion. In vertebrates, core cohesin subunits exhibit prominent ChIP peaks at CTCF sites[46–48], where loop extrusion is blocked. However, cohesin ChIP-seq also exhibits diffuse signal between CTCF peaks, which may reflect true translocating cohesin or non-specific background from the antibody[49]. This ambiguity complicates quantifications, as exemplified by antibodies against distinct cohesin subunits yielding markedly different fractions of reads at CTCF peaks (12% for RAD21 antibody vs. 5% for SMC1A antibody, Fig. 4A-B).

To determine how much of the detected ChIP signal is due to nonspecific antibody binding, we performed spike-in calibrated cohesin ChIP after cohesin depletion (Fig. 4B). We depleted RAD21 with an auxin-inducible degron[50–52] for 3.5 hours (Extended Data Fig. 6A-B) and performed ChIP-seq for RAD21 and SMC1A. This allowed quantifying and subtracting the antibody background from the ChIP-seq signal obtained in cells with normal cohesin levels. Using this approach, we found that only ~25% of the cohesin ChIP-seq signal is in the 0.8% of the genome bound by CTCF (Fig. 4B). This background subtraction procedure yielded strong concordance between the RAD21 and SMC1A antibodies, despite their different specificities prior to correction (Fig. 4B). We note that 25% is an upper bound for the fraction of cohesin binding in CTCF peaks, as signal remaining after auxin treatment also includes any undegraded bound cohesin (less than 4%, Extended Data Fig. 6A-B). Thus, the majority of cohesin molecules are positioned between CTCF peaks, where they are likely engaged in extrusion, transiently bound at loading sites, or stalled by collisions or other barriers, such as the transcriptional machinery.

Cohesin enrichment at NIPBL/MAU2 sites was only ~2-fold over background (Fig. 4C; Extended Data Fig. 6C-D), and most NIPBL/MAU2 peaks did not coincide with RAD21 peaks (Extended Data Fig. 1F). Since our simulations indicated that isolated loading sites are not expected to retain cohesin, we next asked whether NIPBL/MAU2 binding at enhancers nonetheless increases cohesin levels in the surrounding chromatin.

Proximity to a NIPBL/MAU2 binding site only mildly boosts cohesin levels

Guided by our simulations, we quantified RAD21 ChIP-seq enrichment at CTCF peaks, reasoning that the cohesin level, normalized to CTCF occupancy, reflects the amount of extruding cohesin blocked at each site. While CTCF and RAD21 signals were correlated, the correlation was lower than between CTCF replicates or between RAD21 replicates (Fig. 5A-B, Extended Data Fig. 6E). Accordingly, the RAD21/CTCF ratio varied 15-fold between sites (Fig. 5C), highlighting that CTCF sites with comparable occupancy block markedly different cohesin amounts across the genome (Fig. 5D). This variability is not simply explained by CTCF motif architecture, as cohesin levels were independent of the presence of upstream or downstream auxiliary motifs beyond the core CTCF motif[53] (Extended Data Fig. 6F).

Proximity to NIPBL/MAU2 sites or enhancers did not appreciably influence the RAD21/CTCF ratio: CTCF peaks within 1 kb of a NIPBL/MAU2 site only showed 1.1-fold higher cohesin enrichment compared to sites over 100 kb away from the nearest NIPBL/MAU2 binding site (Fig. 5E). We reached the same conclusion by analyzing ChIP-seq from neural progenitor cells (NPCs, Extended Data Fig. 7A-B), indicating that NIPBL/MAU2 binding sites only have a minimal influence on the amount of cohesin that extrudes to neighboring CTCF sites.

As an orthogonal measure, we inspected whether NIPBL/MAU2 binding sites create chromatin folding signatures expected from targeted cohesin loading, such as Hi-C fountains or stripes[25–27,29,30] (Extended Data Fig. 5B). Individual strong NIPBL/MAU2 sites did not display such patterns (Extended Data Fig. 8A), although a weak fountain-like signal is present in aggregate heatmaps[25] (Extended Data Fig. 8B). This observation further supports that cohesin loading at NIPBL/MAU2 sites does not have a major role in shaping chromosome folding patterns in ESCs.

Altogether, our analyses indicate that the cohesin that loads at enhancers is not a major contributor to the flux of loop extrusion. Because other studies reported that enhancer insertions can increase cohesin levels at nearby CTCF sites[8,11], we considered alternative mechanisms by which enhancers could increase cohesin flux. One possibility is that, instead of acting as direct loading sites, enhancers could increase cohesin recruitment over their broader genomic neighborhood, for example by shifting chromatin domains into an accessible state more permissive to loading. Consistent with this idea, simulations showed that increasing diffuse loading over a 50 kb domain by only 2-fold enriches cohesin at flanking CTCF sites as effectively as increasing targeted loading at a single site 500-fold (Fig. 3D and Extended Data Fig. 5D). Thus, our genomic analyses are consistent with a model where enhancer activation triggers modest, domain-wide modulation of cohesin loading that elevates extrusion flux, without necessarily acting as the direct initiation sites for extrusion.

Active Transcription and clustered CTCF sites impede cohesin traffic

Together, our experimental observations and simulations demonstrate that targeted loading can only explain a small portion of the 15-fold variation in cohesin enrichment measured at CTCF sites (Fig. 5). We therefore investigated to what extent this heterogeneity in cohesin traffic arises from the location of extrusion barriers, rather than cohesin loading.

Intragenic CTCF sites retained the least cohesin when most highly transcribed (Extended Data Fig. 9A), with the lowest cohesin retained at CTCF motifs oriented in the direction of transcription (Extended Data Fig. 9B). This pattern is consistent with transcribing polymerases as mobile barriers that push cohesin during elongation[9,12,31,54–56], particularly when cohesin can translocate in the direction of transcription without encountering an opposing CTCF.

Cohesin accumulation at CTCF sites was also distinctly influenced by the density and orientation of CTCF binding. CTCF sites within 1 kb of another site bound ~1.7-fold less cohesin than isolated sites (>1 Mb apart), in both ESCs (Fig. 6A) and NPCs (Extended Data Fig. 7D). Analysis of tandemly oriented CTCF pairs revealed orientation and spacing-dependent effects, with the most pronounced reduction in cohesin accumulation at sites within 30 kb downstream of a co-oriented site (Fig. 6B and 6C, Extended Data Fig. 7E).

To further explore the mechanistic basis of these genomic correlations, we turned to simulations. We modeled CTCF sites as dynamic barriers where the average occupancy of a site is determined by the duration of CTCF binding (bound time) and the interval between binding events (unbound time)[45]. In simulations of a pair of tandemly oriented CTCF sites, cohesin at the downstream site was reduced up to three-fold when the barriers were immediately adjacent, and increased sharply with increasing spacing (Fig. 6D). High occupancy sites (with longer bound time) blocked most effectively. These results support that barrier interference contributes to the variation of cohesin levels at CTCF sites across the genome.

To explore the interference between CTCF barriers within complex genomic layouts, we simulated a chromosome with many randomly positioned CTCF sites with a range of CTCF occupancies. The resulting cohesin/CTCF ratios showed wide dispersion, with closely spaced CTCF sites retaining the lowest amount of cohesin, recapitulating the patterns seen in ChIP-seq data (Fig. 6E, Extended Data Fig. 10 and 11). Varying either CTCF bound time or unbound time resulted in a wide range of cohesin/CTCF ratios (Extended Data Fig. 10A-B). By contrast, regularly spaced CTCF arrays produced a narrower range of cohesin/CTCF ratios, even when using CTCF sites of variable occupancies (Fig. 6E, Extended Data Fig. 10). These simulations

highlight how configurations with clustered barriers can substantially suppress cohesin traffic beyond the effect of any individual site.

Finally, we asked whether such sequence-encoded interference is captured by predictive machine learning models that are mechanism-agnostic. Using Enformer (Avsec et al., 2021), we found that introducing CTCF sequences with high cohesin binding into a recipient locus with flanking CTCF sites lowered predicted cohesin levels, mirroring experimental patterns (Extended Data Fig. 12). Removing the flanking CTCF motifs abolished this effect, illustrating that even sequence-based models implicitly capture interference between neighboring CTCF sites.

Altogether, these findings reveal that genome-wide cohesin positioning is shaped more by interference between extrusion barriers – arising from transcription and clustered CTCF sites – rather than by targeted loading, providing a simple explanation for the wide dispersion of cohesin levels at CTCF sites across the genome.

Discussion

Together, our findings argue against a model in which targeted cohesin loading at enhancers increases their functional interactions with distal promoters to boost transcription. Indeed, we observed that, at a locus that relies on loop extrusion for enhancer-promoter communication, increasing cohesin loading at the enhancer represses transcription from the target promoter 170 kb away. Recent studies have also reported that targeted cohesin loading causes transcriptional repression of neighboring promoters[41], not activation – even at physiological loading rates from endogenous enhancers[30].

Our analyses highlight that, as enhancers only constitute a small fraction of the genome, their contribution to overall cohesin on chromosomes is overshadowed by baseline loading across the rest of the genome, even with high loading rate at enhancers (Extended Data Fig. 13). Yet, our results do not rule out that, in specialized genomic or cellular contexts, focal loading at some enhancers could modulate interactions with neighboring promoters in a functionally relevant way. Indeed, small changes in enhancer-promoter contact frequency can meaningfully affect transcription – especially when the baseline contact frequency is low[57]. Focal loading at the enhancer could increase interactions with a promoter if cohesin remained anchored at the enhancer due to an additional factor such as CTCF binding[8,10,58], possibly RNA polymerase[12,31], or, speculatively, factors that may inhibit direction switching of extrusion[59]. However, most ESC enhancers do not display chromosome interaction patterns (fountains) that would be indicative of elevated interactions. Our observations indicate that long-range transcriptional regulation largely operates without relying on cohesin loading and loop initiation at enhancers, even at cohesin-dependent loci.

Several studies have demonstrated that enhancers can influence the local cohesin flux and genome folding, raising the question of how such effects can be reconciled with their minimal contribution to overall cohesin loading. Our observations are consistent with a model where enhancers modulate cohesin levels indirectly, by increasing loading across an entire domain rather than acting as discrete initiation sites for extrusion. Consistent with this view, our simulations show that modest increases in domain-wide loading produce substantially larger

effects on cohesin accumulation at CTCF sites than even stronger focal loading. These simulations of a broad, but not focal, boost in cohesin loading can quantitatively account for the observation that inserting an enhancer in a silent domain leads to a three-fold increase in cohesin at a CTCF site over 100 kb away[8]. Furthermore, studies in different cell types have found that inserting an enhancer can create a new self-interacting domain and increase cohesin binding at sites across the domain[8,60]. Additionally, regions with enhancers or other markers of active chromatin display higher domain-wide interactions[26,61], and regain domain-wide self-interactions faster after transient cohesin depletion[62]. Studies in yeast demonstrated that chromatin remodelers can recruit NIPBL/MAU2[63], suggesting that more accessible chromatin domains may experience more pervasive cohesin loading.

The idea of mammalian enhancers facilitating domain-wide rather than focal cohesin loading remains compatible with observed Hi-C fountains. Fountains in differentiated mammalian cells[26] emerge from active regions hundreds of kb in width that are surrounded by heterochromatin. Such fountains are not evident at ESC enhancers in baseline conditions[25] (Extended Data Fig. 8) - perhaps due to the generally open chromatin of ESCs[64], which could result in more uniform cohesin loading. However, the fountains that appear in ESCs after depletion of CTCF and the cohesin unloader WAPL are similarly located at multi-kilobase active domains flanked by heterochromatin[29]. Altogether these considerations are consistent with active enhancers inducing recruitment of cohesin across the width of the active domain, rather than acting as the direct initiation sites of extrusion.

Our analyses illustrate how even modest increases in pervasive, domain-wide cohesin loading can substantially elevate the local flux of loop extrusion. By increasing domain-wide cohesin loading, enhancers could increase chances of transient but functionally productive encounters with distal promoters[65], without the need to directly initiate cohesin loading at levels that risk interfering with transcription (Fig. 1A).

In this context, the functional relevance of NIPBL enrichment at regulatory elements remains to be clarified. NIPBL binding at enhancers has been consistently reported across studies in various cell types[15,66–68], while NIPBL binding at promoters was only reported by some[15,17,38,54,66,67] but not all[31] studies. Our observation that NIPBL binding is enriched at enhancers over promoters in ESCs is explained because most pluripotency transcription factor binding sites are distal to promoters[69], while in other cell types, NIPBL binds with transcription factors that are found at promoters[38]. NIPBL recruitment likely occurs through direct interactions with cell-type specific transcription factors[70] or via intermediate co-factors present across cell types, such as Mediator[15,71], BRD4[72], or the transcription complex itself[73]. Whether NIPBL has cohesin-independent functions at regulatory elements and whether NIPBL/MAU2 ChIP-seq peaks depend on cohesin loop extrusion requires further clarification, as studies have reported conflicting results[31,41].

Regarding the presence of cohesin at enhancers, many studies, especially in differentiated cells, reported low but detectable cohesin enrichment at enhancers[5,6,10,15–17,66,68,74–76]. Given our results, extrusion blocking emerges as a more plausible explanation than targeted loading for cohesin enrichment at such lineage-specific transcription factor binding sites[77]. Supporting a blocking-based mechanism, deletion of transcription factor binding sites within an embryonic stem cell enhancer increases cohesin traffic toward neighboring CTCF sites[78], and polymer

simulations better reproduce chromosome folding pattern by implementing blocking rather than simply loading at enhancers alone[12,77].

Several non-exclusive mechanisms can be envisioned for how enhancers may block cohesin (independently of CTCF). First, the transcription machinery itself can act as a barrier to cohesin extrusion[9,12,31,56]. Second, extrusion may halt upon direct or indirect interaction between cohesin and factors or structures present at regulatory elements. For example blocking at TSSs could be mediated by the chromatin reader protein Phf2, which translocates with cohesin and may arrest extrusion upon binding H3K4me3[79]. Finally, blocking may arise from indirect physical constraints. For example, transcriptional condensates have been reported to exert forces on DNA *in vitro* of up to 7pN[80], far exceeding the force sufficient to stall extrusion (~0.1-0.4 pN, [81]), providing a potential explanation for the low-level and diffuse cohesin enrichment detected by ChIP-seq at enhancers, without the need to invoke direct TF-cohesin interactions[18]. The mechanisms of cohesin blocking at enhancers and the relevance in long-range regulation remain to be investigated.

Our quantitative analyses of cohesin ChIP-seq reveal that most molecules (>75%) are found outside CTCF sites. This result is consistent with orthogonal imaging measurements indicating that TADs are rarely fully extruded even at steady-state[82–85]. By extracting interpretable signatures of extrusion dynamics from snapshot cohesin ChIP-seq, our work explains why cohesin occupancy is a better predictor of 3D genome folding patterns than CTCF occupancy alone[86]: the impact of a CTCF site on cohesin traffic depends on the amount of the extrusion flux it can intercept, which itself depends on the density, orientation, and binding kinetics of nearby CTCF sites. These considerations are directly relevant to the interpretation of CTCF site disruptions (with mutations of isolated CTCF sites producing larger chromosome folding defects[43,87–89]) and developmental loci where tuning cohesin trajectories implements cellular decisions[33,90,91].

Finally, our work does not exclude functional roles for targeted cohesin loading, especially in genomic processes beyond enhancer regulation. For example, targeted increases in cohesin loading have been proposed to guide DNA double-strand break repair by non-homologous end joining[92], a process accompanied by local transcriptional suppression[93]. We speculate that DNA break-induced targeted cohesin loading may contribute to the local suppression of transcription. In *S. cerevisiae,* targeted loading of condensin, another loop extruder, guides recombination events underlying mating type switching[94].

Taken together, our work reframes the relationship between transcriptional regulatory elements and cohesin biology, illuminating how genomic context shapes the local flux of loop extrusion within which enhancers operate.

415 **Methods**
416
417 **Plasmid Construction**
418 Plasmids were assembled using Gibson assembly (NEB HiFi DNA Assembly Master Mix
419 E2621) or restriction-ligation (NEB Quick Ligase M2200). A list of all plasmids used in this
420 study is available in Supplementary Table 1 and 2.
421
422 **Cell culture**
423 Parental wild-type E14Tg2a (karyotype 19, XY, 129/Ola isogenic background) *Mus*
424 *musculus* embryonic stem cells and subclones were cultured in 2iSL medium [DMEM +
425 GlutaMAX + sodium pyruvate (ThermoFisher 10569044) supplemented with 15% fetal bovine
426 serum (Gibco SKU A5256701), 550 µM 2-mercaptoethanol (ThermoFisher 21985-023), 1X
427 nonessential amino acids (ThermoFisher 11140-050), 10^4 U/mL of Leukemia Inhibitory Factor
428 (Millipore ESG1107), 1 µM PD0325901 (Apex Bio/Fischer A3013-25), and 3 µM CHIR99021
429 (Apex Bio/Fischer A3011-100)]. Cells were maintained at a density of 0.2-1.5 x 10^5 cells/cm^2 by
430 passaging using TrypLE (ThermoFisher 12605010) every 1-2 days on 0.1% gelatin-coated dishes
431 (Sigma-Aldrich G1890-100G in 1XPBS) at 37°C and 5% CO_2. The medium was changed daily
432 when cells were not passaged. Cells were checked for mycoplasma infection every 6 months and
433 tested negative.
434 To establish neural progenitors (NPCs), 0.2 million WT E14 or NIPBL-FKBP ESCs were
435 seeded in a gelatinized T25 flask in 2iSL medium. The following day, cells were rinsed twice in
436 1X PBS and switched to N2B27 medium [50% DMEM/F12 medium (Gibco 31330-038), 50%
437 Neurobasal medium (Gibco 21103-049), 1X GlutaMAX (Gibco 35050061), 0.5X B27 (Gibco
438 17504-044), 0.5X N2 (Millipore SCM012), and 0.1 mM 2-mercaptoethanol], and media was
439 changed daily. After 7 days, cells were detached using TrypLE, seeded in nongelatinized
440 bacterial dishes for suspension culture at 3 million cells per 75 cm^2, and cultured in N2B27
441 containing 10 ng/mL EGF and FGF (Peprotech 315-09 and 100-18B). After 3 days, floating
442 aggregates were seeded on gelatinized dishes. After 2-4 days, poorly attached aggregates were
443 dislodged and discarded, and remaining adherent NPC cells were dissociated using Accutase
444 (Innovative Cell Technologies AT104), passaged twice on gelatinized dishes in N2B27 +
445 EGF/FGF and cryopreserved after expansion in 10% DMSO in N2B27 + EGF/FGF. Cells were
446 thawed and cultured on gelatinized dishes in N2B27 + EGF/FGF and passaged using Accutase
447 for 2-3 minutes at room temperature.
448 $FKBP^{12F36V}$ depletion was triggered by adding PROTAC dTAG-13 (dTAG) (Sigma-
449 Aldrich SML2601) to a final concentration of 500 nM. AID depletion was triggered by adding
450 indole-3-acetic acid sodium salt (IAA, auxin analog) (Tocris Bioscience 7932) to a final
451 concentration of 500 mM.
452 HEK cells were grown in DMEM with 10% FBS and split when 70% confluent using
453 TrypLE. The medium was changed every 2-3 days.
454 U2OS cells were grown in McCoys 5A media (Thermo Fisher 16600082) supplemented
455 with 10% FBS at 37°C and 5% CO2. Cells were passaged every 2-3 days when 70-80%
456 confluent using TrypLE.
457
458 **ESC Genome engineering**
459 For transfection, plasmids were prepared using the Nucleobond Midi kit (Macherey
460 Nagel 740410.5). Transfections were done using the Neon system (Thermo Fisher) with a 100

461 µL tip and 1 million cells at 1400 V, 10 ms, 3 pulses. To create knock-in cells, ESCs were co-
462 transfected with 5 µg of vector expressing Cas9 and sgRNA and 20 µg of targeting construct.
463 Homology arms of targeting vectors were ~1 kb. For deletions, 2.5 µg each of two sgRNAs
464 targeting the two ends of the deletion were used.
465 After electroporation, cells were seeded in a 9 cm^2 well and left to recover for 48 hours.
466 Cells were then plated at limiting dilution and grown for 8-11 days, changing medium every
467 other day, until single colonies could be picked. Individual colonies were genotyped by PCR and
468 validated with Sanger sequencing.
469 When the targeting construct contained a resistance cassette, sgRNAs were cloned into
470 pX330, for co-expression of the sgRNA and Cas9. Cells were grown with antibiotic in the
471 medium from the time of serial dilution until the colonies were picked (Puromycin: 1 µg/mL;
472 Hygromycin: 200 µg/mL).
473 When the targeting construct did not contain a resistance cassette, we used sgRNAs
474 cloned into a Cas9-2A-puro vector (pEN243, identical to pX459 Addgene 62988). Cells were
475 treated with puromycin from ~24-72 hours after transfection to kill untransfected cells.
476 For mESC experiments using lipofectamine transfections, 360 ng total of plasmid was
477 mixed with 150 ul OptiMEM, and separately 1.8 ul lipofectamine 2000 was mixed with 150 ul
478 OptiMEM. Both mixtures were incubated in the dark for 5 minutes, then combined and
479 incubated for an additional 60 minutes in the dark at room temperature. 300 ul of the mixture
480 was then added to 0.3 million ESCs seeded in a 9 cm^2 well. A list of all cell lines used in this
481 study is available in Supplementary Table 3.
482
483 **HEK cell genome editing**
484 We created a HEK cell line in which the C-terminal of CTCF is tagged with a series of
485 epitopes (HA-FLAG-TY1-eGFP-T2A-PuroR). For genome editing, 1 million cells were
486 transfected with 20 ug of the targeting construct and 5 ug of the Cas9 sgRNA plasmid. We used
487 the Neon system with a 100 µL tip at 1100 V, 20 ms, 2 pulses. After transfection, the cells
488 recovered for four days, with 1 µg/mL puromycin added starting two days after transfection.
489 Four days after transfection, the cells were split, diluted, and dispensed into 96-well plates at a
490 concentration such that there was an average of 0.5 cells per well. After 10 days of growth, single
491 colonies were genotyped by PCR. Of 27 colonies, 10 appeared homozygous for the insertion,
492 and the remainder heterozygous for the insertion. The insertion was verified by sequencing, and
493 GFP expression was confirmed by flow cytometry.
494
495 **Western blotting**
496 We used Western blotting to quantify RAD21 and MAU2 depletion. Approximately 10
497 million ESCs were dissociated using TrypLE, resuspended in culture medium, and pelleted at
498 100g for 5 minutes at room temperature. Cell pellets were washed in PBS, pelleted again, snap
499 frozen on dry ice after aspirating the PBS, and stored at −70°C. Cell pellets were resuspended in
500 10 mM HEPES (pH 7.9), 2.5 mM MgCl2, 0.25 M sucrose, 0.1% NP40, 1 mM DTT, and 1X
501 HALT protease inhibitors (ThermoFisher 78437) and kept on ice for 10 minutes to allow
502 swelling. After centrifugation at 500g at 4°C for 5 minutes, the supernatant was discarded and
503 the pellets were resuspended on ice in 25 mM HEPES (pH 7.9), 1.5 mM $MgCl_2$, 700 mM NaCl,
504 0.5 mM DTT, 0.1 mM EDTA, 20% glycerol, 1 mM DTT, and 250 U benzonase (Sigma-Aldrich
505 E1014), and incubated on ice for 10 minutes. The nuclear lysates were centrifuged at 18,000g at

506 4°C for 10 minutes, to eliminate the cellular debris. Protein concentration from the supernatants
507 was measured using Pierce BCA Kit (ThermoFisher 23225).
508 40 ug of protein extract was combined with 1x Laemmli buffer (Biorad 1610747), heated
509 at 95°C for 10 minutes, and subjected to electrophoresis on a 4-15% polyacrylamide gel (Biorad
510 17000927). The separated proteins were transferred onto a polyvinylidene difluoride (PVDF)
511 membrane (Millipore IPFL00010) using phosphate-based transfer buffer (10 mM sodium
512 phosphate monobasic, 10 mM sodium phosphate dibasic) at 4°C, 600 mA, for 1.5 hours. After
513 the transfer, the membrane was cut so the lower molecular weight section could be blotted with
514 TBP antibody for the loading control. Membranes were blocked in 5% blocking buffer (5% skim
515 milk in TBS-T (20 mM Tris-Cl buffer-pH 7.4, 500 mM NaCl and 0.1% Tween 20)) and
516 incubated overnight at 4°C with the primary antibodies (RAD21 Millipore 05-908 1:1000,
517 RAD21 abcam ab154769 1:1000, MAU2 abcam ab183033 1:1000, or TBP Cell Signaling
518 Technology 8515S 1:2000) prepared in 5% blocking buffer. The next day, the membranes were
519 washed three times with TBS-T buffer and incubated with mouse or rabbit secondary antibodies
520 conjugated with horseradish peroxidase diluted 1:2000 (Biotium 20400, Biotium 20403) for 1 hr
521 at room temperature. The membranes were again washed three times with TBS-T buffer. The
522 blots were developed using Pierce ECL western blotting substrate (ThermoScientific 32209) and
523 detected using Chemidoc XRS+ imager (Biorad).
524 Three biological replicates of untagged (E14) and RAD21-GFP-AID cells with and
525 without auxin treatment were collected on separate days. Intensity of the bands was quantified
526 using ImageJ. For Extended Data Fig. 6A, RAD21 intensities were normalized to TBP and then
527 to the value in untagged cells.
528
529 **Flow cytometry**
530 ESCs were dissociated with TrypLE, resuspended in culture medium, pelleted, and
531 resuspended in 10% FBS in PBS before live cell flow cytometry on an Attune NxT instrument
532 (Thermo Fisher). Analyses were performed using the FlowJo software. Briefly, live cells were
533 gated using FSC-A x SSC-A and singlets were then gated using FSC-H x FSC-A before
534 extracting median values for approximately 50,000 final gated cells. The value of
535 autofluorescence in untagged E14 cells was subtracted.
536 For quantification of RAD21-GFP, values were normalized by dividing by the average
537 expression in untreated cells, and replicates were obtained by collecting cells on different days.
538
539 **Calibrated ChIP-seq**
540 For all NIPBL and MAU2 ChIP experiments, cells were double crosslinked in
541 disuccinimidyl glutarate (DSG) followed by formaldehyde. First, cells were dissociated using
542 TrypLE (ESCs) or Accutase (NPCs) and resuspended in culture medium. 15 million cells were
543 pelleted at 100*g* for 5 minutes at room temperature. Supernatant was discarded and cell pellets
544 were washed once in PBS. Cells were resuspended in 10 mL PBS, and DSG (Fisher Scientific
545 AAH58208MC) dissolved in DMSO was added to a final concentration of 2 mM. Cells were
546 fixed at room temperature for 45 minutes with rotation. Cells were then pelleted at 200*g* for 5
547 minutes and washed three times with PBS (each time pelleting at 200*g* for 5 minutes). Cells were
548 then resuspended in 5 mL of 10% FBS prepared in PBS. To this, 5 mL of freshly prepared 2%
549 formaldehyde solution was added to reach a final formaldehyde concentration of 1%. 2%
550 formaldehyde was diluted from 16% methanol-free formaldehyde (Fisher Scientific PI28908) in
551 1X PBS with 10% FBS. Resuspended cells were fixed in formaldehyde for 10 minutes at room

552 temperature with rotation. To quench, 0.525 mL of 2.5 M glycine (Millipore Sigma GX0205-1)
553 solution in PBS was added (final concentration 0.125 M glycine), and cells were incubated for 5
554 minutes at room temperature followed by 15 minutes on ice. Cells were pelleted by centrifuging
555 at 200*g* for 5 minutes at 4°C. Cell pellets were resuspended in 1 mL of ice-cold 0.125M glycine
556 in PBS, transferred to 1.5 ml tubes, and centrifuged at 300*g* for 5 minutes at 4° C. Supernatant
557 was discarded and pellets were snap frozen on dry ice and stored at -70°C.
558 For CTCF and RAD21 ChIP, cells were dissociated, pelleted, and fixed in 1%
559 formaldehyde for 10 minutes with the subsequent quenching and washes as above.
560 For ChIP, fixed cells were thawed on ice, resuspended in 1 mL of ice-cold lysis buffer [10
561 mM Tris-HCl pH 7.5, 10 mM NaCl, 0.2% NP-40 (IGEPAL), 0.2% TritonX-100, 1 mM EDTA,
562 0.5 mM EGTA, supplemented with fresh 1x protease inhibitor (Thermo Scientific PI78437)] and
563 incubated on ice for 10 minutes. ~9.75 x 10^6 mouse nuclei were combined with ~0.25 x 10^6 fixed
564 HEK nuclei as spike-in. For ChIP experiments with HA antibody, HEK cells with an HA epitope
565 (cell line EA46.3) were used for the spike-in. Nuclei were pelleted at 400*g* for 5 minutes at 4°C,
566 the supernatant was discarded, and nuclear pellets were resuspended in 1 mL of shearing buffer
567 (0.5% SDS, 10 mM Tris-HCl pH 7.5, supplemented with fresh protease inhibitor). Chromatin
568 was sheared using an S220 Covaris with settings PIP 105, duty factor 5, cycles per burst 200,
569 total time 23 minutes for double-crosslinked cells or 15 minutes for formaldehyde-crosslinked
570 cells. After shearing, samples were spun at 13,000 rpm for 5 minutes at 4° C. 2.5% of the sample
571 was removed to use as input, and the remainder of the supernatant was used for ChIP. The ChIP
572 reaction was assembled as follows: 900 ul chromatin, 442 μL 5X ChIP incubation buffer (5%
573 TritonX-100, 0.75 M NaCl, 5 mM EDTA, 2.5 mM EGTA, 50 mM Tris-HCl pH7.5), 40 uL
574 Dynabeads (pre-rinsed in ChIP incubation buffer), 10 ug antibody, 22.5 uL protease inhibitor,
575 and 835.5 uL water. Tubes were incubated overnight at 4°C on a rocker.
576 The following antibodies were used for ChIP: HA (Thermo Fischer 26183), RAD21
577 (Abcam ab992), RAD21 only for experiments in RAD21-AID cell lines (abcam ab154769),
578 CTCF (Active Motif 61311), NIPBL (Bethyl A301-779A), H3K27ac (abcam ab4729).
579 Following overnight incubation, beads were collected using a magnetic rack and washed
580 sequentially with different chilled wash buffers for 5 minutes each on a rocker at 4°C. Beads
581 were washed twice with 500 μL of wash buffer 1 (0.1% SDS, 0.1% Sodium deoxycholate, 1%
582 TritonX-100, 0.15 M NaCl, 1 mM EDTA, 0.5 mM EGTA, 10 mM Tris pH 8), once with 500 μL
583 of wash buffer 2 (0.1% SDS, 0.1% Sodium deoxycholate, 1% TritonX-100, 0.5 M NaCl, 1 mM
584 EDTA, 10 mM Tris pH 8), once with 500ul of wash buffer 3 [0.25 M LiCl, 0.5% Sodium
585 deoxycholate, 0.5% NP-40 (IGEPAL), 1 mM EDTA, 0.5 mM EGTA, 10 mM Tris pH 8], and
586 twice with 500 μL of wash buffer 4 (1 mM EDTA, 0.5 mM EGTA, 10 mM Tris pH 8).
587 To elute the DNA, beads were resuspended in 200 μL of elution buffer (1% SDS, 0.1M
588 $NaHCO_3$) and incubated on a rocker for 20 minutes at room temperature. Beads were then
589 separated using a magnetic rack, and the eluate was transferred to a fresh tube while beads were
590 discarded. Input samples were thawed and elution buffer was added to bring the volume to 200
591 μL. 2 μL of 1 mg/ml RNaseA (Thermo Scientific FEREN0531) was added before incubation at
592 37°C for 30 minutes. To reverse crosslinks, 8 μL of 5 M NaCL and 5 μL of 10 mg/ml Proteinase
593 K were added, and samples were incubated overnight at 65°C. DNA was eluted using a MinElute
594 kit (Qiagen 28604).
595 Libraries were prepared using NEBNext Ultra II DNA library prep kit according to the
596 manufacturer's protocol (E7645S). The entire ChIP sample and 50 ng of the input samples were
597 used for library prep. Libraries were amplified for 16 cycles, followed by 0.9X SPRI bead

598 purification (Bulldog Bio CNGS005). The eluate was run on a 2% E-gel (Invitrogen G401002)
599 and fragments between 200-600 bp were excised and eluted using a MinElute gel extraction kit
600 (Qiagen 28604). Quality and quantity of libraries were assessed using Qubit and Bioanalyzer
601 High Sensitivity DNA kit (Agilent 5067-4626). Libraries were sequenced on a NextSeq 2000
602 using 65 bp single-end reads. Some libraries were sequenced in a second lane for additional
603 reads. Each replicate is a population of cells fixed on a separate day.
604
605 **ChIP-seq mapping**
606 Reads from fastq files were aligned to a catenated mm10 and hg38 reference genome
607 using Bowtie2. Reads with a mapq score ≥ 30 were retained and duplicates were removed, using
608 samtools version 1.21 ref[95]. ChIP bigwigs were generated with the bamCoverage function from
609 deepTools[96], with scaling factors calculated using the formula (human reads in input) / (mouse
610 reads in input) / (human reads in ChIP) x 15,000,000 ref[97]. The multiplier of 15,000,000 was
611 chosen arbitrarily to set the final scaling factors close to 1. Input bigwigs were normalized using
612 RPKM. Bigwigs were visualized using the UCSC genome browser[98].
613 To create bigwig files with multiple replicates combined, we took equal numbers of reads
614 from each replicate (samtools view with subsample option), combined them, and generated a
615 bigwig normalized by RPKM.
616
617 **Creating consensus ChIP-seq peak lists**
618 To create lists of ChIP-seq peaks found in multiple replicates, we first used macs2
619 version 2.2.9.1[99] to call peaks on each individual ChIP replicate. For NIPBL and MAU2 peaks,
620 we used HA ChIP in untagged cells as the control. For CTCF and H3K27ac peaks, we used the
621 corresponding input sample as the control. We used bedtools multiinter to identify regions that
622 were called as peaks in the majority of replicates. To define the peak widths, we again called
623 peaks using macs2, this time including all of the replicates together. Using bedtools intersect -u,
624 we selected the peaks from the list called using combined replicates that overlap with the regions
625 called in the majority of replicates. Finally, we removed peaks in ENCODE blacklisted
626 regions[100] using bedtools intersect -v.
627 All analyses of NIPBL/MAU2 peaks use the consensus list of HA-MAU2 peaks, as the
628 HA-MAU2 ChIP was more sensitive compared to the HA-NIPBL ChIP.
629
630 **Comparing ChIP-seq binding**
631 We generated tornado plots and plots of average binding at ChIP-seq peaks using
632 computeMatrix and plotHeatmap functions from deepTools. OCT4 ChIP-seq is from ref[51], file
633 name GSM3992929_33_WaplC6-0h_antiOct4.bw, and H3K4me3 ChIP-seq is from ENCODE
634 mouse ES-E14 dataset ENCSR000ADL, file ENCFF001MXU, both mapped to mm10 as above.
635 We used the H3K4m3 peak list ENCFF012AZO. We generated the upset plot (Extended Data
636 Fig. 1E) using Intervene[101].
637
638 **TetO array imaging**
639 We recruited transcription factors to a TetO array in U2OS 2-6-3 cells[40]. We avoided
640 using the LacO repeats that are also present in the array as we observed that LacR expression
641 alone led to cohesin recruitment, possibly because of chromosomal instability triggered by the
642 tighter LacO-LacR binding[102]. In eight-well ibidi slides (Fisher 50305795), we seeded 20,000
643 cells per well and transfected with a plasmid expressing either TetR-VP64 (pEM037), TetR-

644 OCT4 (pEM040), TetR (pEM041), or TetR-MAU2 (pAA014) using lipofectamine 3000 (Thermo
645 Fisher L3000008) according to the manufacturer's instructions.
646 For immunofluorescence, we rinsed cells once with 250 uL of PBS and then fixed in 3%
647 formaldehyde (Electron Microscopy Sciences 15686) diluted in PBS for 10 minutes at room
648 temperature. Cells were rinsed three times with PBS and permeabilized with fresh 0.5% Triton
649 X-100 in PBS for 5 minutes. After rinsing three times with PBS, cells were incubated with 1%
650 BSA in PBS for 10 minutes. Next, cells were incubated in a 150 uL volume of primary antibody
651 diluted 1:300 in 1% BSA in PBS for 45 minutes (antibodies: NIPBL Bethyl A301-779A, MAU2
652 abcam ab183033, RAD21 Millipore 05-908). Cells were washed five times with 250 uL PBS for
653 5 minutes each. Next, cells were incubated with secondary antibody diluted 1:1000 in 1% BSA
654 in PBS for 45 minutes (goat anti-rabbit Invitrogen A-11012, goat anti-mouse Invitrogen A-
655 11005) and again washed three times. Finally, cells were incubated with 1 ug/mL DAPI in PBS
656 for 5 minutes and rinsed twice in PBS. All steps were performed at room temperature.
657 Images were acquired using a Zeiss spinning disk confocal microscope with 60x
658 objective or Nikon spinning disk confocal microscope with a 60x objective with XY pixel size of
659 183 x 183 nm and 300 nm steps in Z. Images were analyzed in ImageJ with the JACoP plugin to
660 calculate the Pearson correlation between red and green channels within a 12 × 12 × 8 X × Y × Z
661 box manually placed on each GFP-positive TetO array. To calculate the intensity of signal at the
662 array compared to background, for each cell we extracted the total signal within a box centered
663 on the array of size 6x6 XY pixels and 4 z slices. We then chose a box outside the array with a
664 representative level of cohesin of size 12x12 XY pixels and the same 4 z slices as the first box.
665 To account for the different box sizes, we computed enrichment at the array as the (array
666 intensity * 4) / (background intensity).
667
668 **TACL**
669 We heterozygously inserted a 34x TetO array at different locations in a cell line in which
670 the two alleles of *Car2* are tagged with tdTomato and mClover reporters. To facilitate
671 distinguishing between the two alleles by ORCA, we first created a 10 kb deletion of a neutral
672 sequence near *Car2* enhancer 2 (chr3:15062000-15072751).
673 We then inserted the 34x TetO array at three locations in the *Car2* locus. To ascertain
674 which allele the TetO array was inserted on, we used a Cas9-based strategy. For the TetO
675 insertion 4 kb upstream of the *Car2* TSS (EA88), we performed a lipofectamine 2000
676 transfection of plasmids encoding Cas9 and sgRNAs to cut in the TetO repeats and downstream
677 of the *Car2* open reading frame. For the TetO insertion 107 kb downstream of the *Car2* TSS
678 (EA89), we used sgRNAs targeting TetO and downstream of the Car2 enhancers. To select
679 transfected cells, we added puromycin and hygromycin from 1 day to 3 days after transfection.
680 Five days after transfection, we performed flow cytometry and observed a population of cells
681 with loss of either red or green expression, indicating which allele experienced large deletions
682 and therefore harbored the TetO array. For the TetO array 172 kb downstream of the *Car2* TSS,
683 we used a PCR strategy relying on the existing 10 kb deletion downstream of the *Car2* enhancers
684 on the red allele.
685 For TACL experiments, cells were transfected with plasmids expressing either TetR-
686 Halo-MAU2 (pAA014) or TetR-Halo (pEA117) using lipofectamine 2000 along with piggyBac
687 transposase plasmid (PB200). Starting two days after transfection, cells were grown in 1 µg/mL
688 puromycin to select for cells with successful integrations. Seven days after transfection, *Car2*
689 reporter expression was measured using flow cytometry. For each location of the TetO

integration, two clones were each transfected three separate times. Flow cytometry measurements were normalized by dividing by the average reporter expression in untransfected cells of the corresponding genotype.

ORCA experiment

Cell lines and fixation

ORCA experiments were performed on clonal cell lines. For each TetO insertion position, we subcloned the pool of cells from one TetR-Halo and one TetR-Halo-MAU2 transfection. We measured Halo expression in individual clones by flow cytometry, and then for each condition selected a single clone with a similar expression level. Cells were incubated with 500 nM Halo ligand JFX646 (diluted in media) at 37°C for 30 minutes, excess ligand was removed by incubating the cells in fresh media for 30 additional minutes, and Halo expression was measured by flow cytometry.

For fixation, we dissociated cells using TrypLE, fixed in 4% formaldehyde for 10 minutes at room temperature, washed four times in PBS (by centrifuging for five minutes at 400g), resuspended in 70% ethanol, and stored at -20°C.

Multiplexed cell labeling

Cells were labeled by adapting a previously published protocol[50,103] with minor modifications. Briefly, 3'-amine-modified oligonucleotides (Integrated DNA technologies) were conjugated to Methyltetrazine-NHS ester. The reaction was performed in sodium borate buffer (50 mM, pH 8.5) with DMSO, and the resulting methyltetrazine-oligos were purified by ethanol precipitation. The final products were resuspended in HEPES buffer.

For cell labeling, approximately 2.5-3 million fixed cells were transferred to protein LoBind tubes and 3X washed using 1% BSA in PBS and resuspended in 1X PBS. The cells were first incubated with 1 mM TCO-PEG4-TFP Ester for 5 minutes at room temperature protected from light. Subsequently, the prepared methyltetrazine-oligos were added and incubated for 30 minutes at room temperature. The reaction was quenched using Methyltetrazine-PEG4-Amine and Tris-HCl for 5 minutes. Labeled cells were washed 2X with 1% BSA in PBS and once with 1X PBS only. Cells were resuspended in 70% ethanol in 1X PBS and stored at -20 °C.

Cell plating and surface barcode normalization

Barcoded cells were pooled at equal ratios by mixing 2-4 µl of each sample in a single tube. A 10-15 µl aliquot of the pooled cell suspension was then dispensed onto the poly-D-lysine coated central region of a microscope slide and left to air dry for ~ 5 minutes before proceeding with primary probe hybridization (see below). Multiple slides were prepared in parallel (4-6), and only those with an optimal cell density forming a uniform monolayer were selected for imaging and backup acquisitions. To assess and even out the representation of all conditions prior to the main imaging experiment, barcoded cells were first imaged using readouts targeting the surface barcodes without DNA primary probe hybridization. The relative abundance of each condition was quantified from these barcode signals, and cell numbers were subsequently normalized accordingly.

Probe design

The *Car2* locus (chr3:14,753,359-15,369,435) was tiled with 72 barcodes spanning 8 kb each, with every barcode targeted by ~120 individual probes. Each probe was 100 bp in length

736 and compromised of 4 segments: 20 bp of a reverse and forward primer sequences used during
737 probe synthesis, 20 bp complementary to the fiducial probes, 20 bp of barcode sequence, and 40
738 bp of unique genomic targeting sequence. Probes were designed using previously described
739 software[104], which is accessible at https://github.com/BoettigerLab/ORCA-public. The probe
740 library was synthesized as an oligonucleotide pool by GenScript.
741
742 *DNA hybridization*
743 Hybridization with DNA primary probes was carried out following[105]. Briefly, following
744 pooling and plating, cells were fixed in 4% paraformaldehyde (PFA) for 10 minutes and washed
745 3X with 1X PBS, which was gently added to the slide by pouring along the side of the 6 cm Petri
746 dish to avoid direct flow over the cells. Cells were then premetallized in 20-40 µl of 0.5% Triton
747 X-100 in 1X PBS for 10 minutes and rinsed 3X with 1X PBS. Permeabilized cells were then
748 incubated in 20-40 µl 0.1 M HCl for 5 minutes and washed 3X with 1X PBS. To remove RNA,
749 cells were treated with 20-40 µl RNase A (10 µg ml^{-1}) for 30 minutes at 37 °C and then washed
750 3X with 2X SSC. Next, cells were equilibrated for 35 minutes in hybridization buffer (2X SSC,
751 50% formamide, 0.1% Tween-20). The volume of solution applied varied depending on the area
752 occupied by cells on each slide; solutions were added in sufficient volume to ensure complete
753 coverage of all cells.
754 Hybridization mixture was prepared by mixing 2 µl of 840 ng $µl^{-1}$ of DNA primary
755 probes and 30 µl hybridization solution (2X SSC, 50% formamide, 10% dextran sulfate, and
756 0.1% Tween-20). The mixture was then applied to the cells, covered with a coverslip treated with
757 Sigmacote, denatured for 3 minutes at 90 °C and then incubated overnight in a humidified
758 chamber at 42 °C. The following day, samples were 3X washed with 2X SSC and post-fix in a
759 mixture of 2% glutaraldehyde (GA) and 8% PFA in 1X PBS for 30 minutes. After post-fixation,
760 slides were 3X washed with 2X SSC and mounted on the microscope for sequential labeling and
761 imaging, starting with surface barcode imaging.
762
763 *ORCA Imaging setup*
764 Imaging was performed using a custom-built ORCA microscope setup with the complete
765 configuration parameters available via MicroMeta App[106]. Briefly, the system was constructed
766 around a Nikon Ti2 body with a large 32 mm aperture optics enabling the acquisition of wide-
767 field images (2,048 x 2,048-pixel area with a final pixel size of 108 nm). Illumination was
768 provided by solid-state laser arrays by Lumencor (CELESTA light engine) paired with a custom
769 polychroic mirror (Chroma, ZET408/473/545/635/750rpc-uf2) and emission filter (Chroma,
770 ZET408/473/545/635/750m). The system was equipped with a Marzhauser Wetzlar xy-stage (00-
771 24-625-000) and a Mad City Labs Inc. Z objective positioner (Nano-F200S) for z-axis control.
772 The setup was completed with a Hamamatsu ORCA-Flash4.0 V3 sCMOS camera, an IR-laser-
773 based autofocus system, and custom fluidics set up[105].
774
775 *ORCA image acquisition*
776 Primary probe hybridized samples were imaged by detecting readout sequences with dye-
777 labeled secondary oligonucleotides: AlexaFluor 750 for DNA readouts, Cy5 for surface barcodes
778 and Cy3 for fiducial markers, with the Cy3 channel used for accurate spatial registration and
779 sample drift correction. Imaging was started with surface barcodes and followed by DNA
780 tracing. Fiducial signals were detected during the first DNA imaging round together with the first
781 DNA readout and were subsequently imaged in every following cycle.

For each readout barcode, ~ 400 µl of probe solution (25% ethylene carbonate in 2× SSC containing the readout oligonucleotide and displacement oligos complementary to the previous readout) was flowed into the chamber and incubated for 30 minutes to allow hybridization and strand displacement. All remaining wash, buffer exchange, and acquisition steps were performed as in the published protocol[105].

ORCA analysis

Raw imaging processing was performed following the image processing pipeline detailed in ref[105] with published scripts available at: https://github.com/BoettigerLab/ORCA-public. This pipeline yields 3D coordinates for every barcode within a given trace, which were subsequently transformed into pairwise distance matrices for structural analysis.

Computational correction for underperforming readouts

To ensure the integrity of population-level data, we computationally corrected all median distance and contact frequency maps for artifacts introduced by specific readout probes. For most of these readouts, the poor performance stems from flawed intrinsic properties, a recurring issue documented in prior ORCA experiments. In this study, a specific list of seven readouts (5, 10, 16, 21, 23, 48, and 65) were identified as unreliable based on visual inspection of the raw imaging data, which revealed issues such as weak signal or spurious fluorescence. The data corresponding to these specific rounds was masked and the resulting gaps in the data matrices were filled by interpolating values from neighboring, high-quality hybridization points.

Readout 38 was masked to account for the 10 kb deletion in the TetO cell lines. While the readout itself performed well, this step prevents the deletion from creating a strong predicted artifact in the differential contact and distance maps for TetO vs. non-TetO conditions.

Demultiplexing cell surface barcodes

Demultiplexing was performed using a custom MATLAB script that integrates Cellpose for nuclei segmentation[107]. For each field of view (FOV), a maximum intensity projection image was generated from the drift-corrected barcode imaging channels to facilitate robust segmentation. Cellpose was then run with its pre-trained 'nuclei' model to generate segmentation masks. For each segmented nucleus, a barcode intensity vector was created by calculating the median pixel intensity within the mask for each barcode channel. These vectors were normalized to account for variations in probe brightness. Finally, each nucleus was assigned an identity by matching its normalized barcode vector to a predefined codebook using a k-nearest neighbor approach, with an associated confidence score calculated to assess assignment ambiguity. The resulting table linked each identified spot from the primary experiment to its parent nucleus and decoded identity.

Allele disambiguation

To distinguish between control allele (non-TetO allele) and allele engineered for forced cohesin loading (TetO allele) via a 10 kb deletion, a custom Python script was used to classify chromosomal traces in each demultiplexed cell based on the presence or absence of imaging readout 38, which specifically hybridizes to the deleted region in the *Car2* control allele. To ensure high confidence in our classification, this comparison was performed exclusively between the two alleles within the same nucleus, which serves as an internal control to mitigate potential misalignment errors or technical false negatives arising from variable hybridization efficiency.

Quantification of enhancer-promoter interactions

Enhancer-promoter interactions were assessed between windows of loci centered around the *Car2* enhancers and promoter. Specifically, we used a +/- 1 bin window for each (P-window, E-window) to account for the physical span of the regulatory elements and to mitigate potential signal dropout from suboptimal probe detection efficiency during imaging.

To avoid using an arbitrary distance cutoff, a data-driven contact threshold was determined as the median of all pairwise distances between adjacent probes measured across the entire traced *Car2* domain in the control cell population, approximately 200 nm across conditions. An E-P interaction was then classified "in contact" for a given cell if the minimum distance between the E and P windows was less than or equal to this threshold.

To capture the full spectrum of interaction distances without binarization, we analyzed the distribution of minimum E-P distances. For each individual cell, we identified the single minimum distance between any locus in the E-window and any locus in the P-window. This metric represents the closest physical approach between the two regulatory regions within that cell.

Simulations

1D lattice model

We performed one-dimensional lattice simulations to model loop extrusion dynamics. Loop extrusion parameters were chosen to reflect mESC dynamics, and the various loading and barrier configurations below were used to probe different determinants of cohesin accumulation. We modeled 1D dynamics with fixed-timestep simulations on a lattice where each lattice site represented 250 base pairs of genomic sequence. All lattice sites shared a uniform unloading (or dissociation) rate for extruders; this is specified via the processivity (330 kb, equivalent to 1320 lattice sites or 660 lattice sites for each arm), the average distance extruded before dissociation. Each site could either represent a generic genomic location with baseline extruder loading probability or be designated as a boosted loading site with increased extruder loading frequency. For standard sites, cohesin loading occurred with uniform probability across the lattice. Average spacing between extruders was determined by a separation parameter, set to 185 kb (740 lattice sites), following experimental estimates[108] and previous simulations[23] in mESC.

Any extruder that dissociated from the lattice was immediately reloaded at a random un-occupied lattice site, where the likelihood of reloading at a given position was proportional to its local loading rate. Each extruder occupied two adjacent lattice sites, corresponding to its left and right legs. At each discrete time step, extruder legs not stalled by a barrier could move outward, (i.e. the left leg moves left and the right leg moves right). For example, an extruder can update from position (i, j) to (i–1, j+1). Extruder legs could not bypass one another upon collision and could not exit the first or last lattice sites, effectively confining all movement within the lattice boundaries. Positions of extruders were recorded after discarding the initial 20% of simulation steps to compute observables.

Dynamic CTCF barriers were implemented as unidirectional obstacles that selectively stalled extruder legs based on their direction of motion (as previously[45]). Dynamic barrier occupancy was modeled as a two-state process, governed by defined binding and unbinding times. Extruders encountering an unbound barrier site continued extrusion uninterrupted. An extruder leg moving in the direction opposite to the orientation of an occupied barrier became

874 stalled upon contact. While one leg was stalled at a bound barrier, the other leg was allowed to
875 continue moving independently.
876
877 *Boosted loading site layouts*
878 Boosted loading was reported as a fold-increase per kilobase. E.g., a loading boost of 100
879 on a 250 bp site is equivalent to a fold-increase of 25 per 1 kb. In simulations involving a single
880 focal loading site, boosted loading was applied at a single 250 bp lattice site. For simulations
881 representing larger loading regions or "active TADs" of uniformly boosted loading, multiple
882 adjacent boosted loading sites were used. In all scenarios, boosted loading added to the total
883 number of extruders in the simulated region. One boosted loading region or site was considered
884 per 1,000 lattice sites. We averaged over 30,000,000 simulation snapshots for these layouts.
885
886 *Quantifying cohesin at the loading site*
887 To quantify the relative enrichment of extruders at boosted target loading sites (Fig. 3B
888 and Extended Data Fig. 5C), we counted extruder reads within a four-site window
889 (corresponding to 1 kb) centered on the center of each boosted target loading region. This local
890 read count was divided by the average number of extruder reads measured in two distal control
891 regions located 20 kb to the left and 20 kb to the right of the target region, using windows of the
892 same size. This value was then normalized to the corresponding value obtained for the uniform
893 loading scenario. The resulting ratio quantifies local extruder enrichment at the boosted loading
894 site while controlling for local background read density.
895
896 *Boosted loading between inward-oriented CTCF layout*
897 To clarify the impact of targeted loading on accumulation at nearby CTCFs, we
898 considered simplified scenarios with isolated CTCF barrier sites oriented inwards symmetrically
899 at a defined distance from a loading site (Fig. 3D, Extended Data Fig. 5). Such arrangements
900 were placed at the center of a 1,000 site region and tiled ten times to form a 10,000-site lattice.
901 For these simplified scenarios, we set the CTCF bound time to be approximately one quarter of
902 the cohesin residence time, reflecting previous estimates[45]. Unless noted, isolated barriers had an
903 occupancy of 0.5, meaning they were CTCF-bound 50% of the time and unbound the other 50%.
904 We calculated an enrichment ratio at CTCF sites as the accumulation of extruder legs at barrier
905 sites in a targeted loading scenario normalized by the baseline from uniform loading. We
906 computed in silico ChIP-seq profiles by recording the positions of extruder legs from 30,000,000
907 instances of 1D lattice simulations for this layout.
908
909 *Tandem CTCF layout*
910 To precisely quantify the impact of nearby CTCF sites arranged in tandem (Fig. 6D), we
911 performed a set of simulations with otherwise isolated tandemly-oriented pairs of CTCF sites. A
912 set of tandem sites were placed at the center of a 1,000 site region and tiled ten times to form a
913 10,000 site lattice. We quantified how the front CTCF can block accumulation at the back CTCF
914 by varying the occupancy of the front CTCF while keeping the back CTCF at 0.5 occupancy. We
915 then calculated RAD21 reads normalized by the number of times each barrier appeared at its
916 genomic position (RAD21/CTCF). We computed in silico ChIP-seq profiles by sampling
917 extruder leg positions from 100,000,000 1D lattice simulation instances.
918
919 *Variable spacing and occupancy of CTCF barriers layouts*

To develop simulations with more complex patterns of cohesin accumulation closer to those in cells, we designed simulations with randomly distributed barriers with variable bound times and occupancies as follows (Fig. 6E, Extended Data Fig. 10) for a lattice with 300,000 sites. Barrier occupancies were independently sampled with replacement from empirical measurements of CTCF binding via single-molecule footprinting[109], and the total number of barriers (multiplied by their occupancy) was chosen to match experimental estimates. Specifically, we sampled barriers until their combined occupancy reached 133 in 10 Mb, based on estimates for the number of bound CTCF molecules in a region of this size (~217,000 total CTCF molecules in a mESC nucleus, with 50% bound (based on FRAP measurements[110]), and an average estimated genomic content per cell ~3 × 2.7 Gb[108]). Lattice positions and orientations were randomly assigned for each sampled barrier. While per site occupancies are available experimentally, per site bound and unbound times are not. Based on previous estimates[45] we thus set these dynamic parameters by scaling sampled bound times such that strong sampled barriers (0.65 occupancy) had a residence time (656 sec) of roughly one third the extruder lifetime, thus fixing their unbound time (353 sec). Average sampled barriers (~.35 occupancy) had a correspondingly lower residence time (233 sec). For varying bound time simulations, we sampled site occupancies, and determined corresponding site bound times using the fixed unbound time (353 sec). We then introduced variability in bound times at fixed sampled occupancies by: drawing an updated bound time from a Gaussian distribution with mean equal to the sampled bound time and standard deviation of ⅓ of the sampled bound time and rescaling the unbound time to maintain the sampled occupancy. For the varying unbound time simulations, a similar rescaling procedure was used, albeit determining site unbound times from the sampled occupancy and a fixed bound time (233 sec). For constant occupancy simulations, all barriers had the same occupancy, and thus the same bound (233 sec) and unbound times (353 sec). For each scenario, we ran 100 independent simulations using multiprocessing, with approximately 153,000 recorded instances per simulation. Statistics were computed by aggregating data across all runs, yielding a total of approximately 15,300,000 simulated instances.

To evaluate the effect of variable separation between barriers on extruder accumulation, we conducted simulations using regular barrier arrangements. First, we maintained the same barrier density (per 10 Mb) and positioned barriers at constant intervals of ~ 35 kb with alternating orientations (right, left, right, etc.). To assess the impact of barrier spacing on the dispersion of cohesin accumulation, we also increased the distance between barriers six-fold.

To quantify cohesin enrichment, we calculated the accumulation of extruders at barrier sites. To compare simulations with experimental data, we scaled both RAD21 and CTCF read counts to match the read densities measured by ChIP-seq. Specifically, we calculated the total number of simulated extruder and CTCF reads per base pair within the 75 Mb simulated region, and applied a normalization factor such that the simulated read density equaled the experimental read density (0.016764 reads per basepair, per haploid genome). This normalization ensured that simulated and experimental datasets had comparable read coverage per genomic length.

To further quantify the role of barrier spacing, we analyzed simulated cohesin positioning at barriers similarly to experimental data. To investigate the role of nearby CTCF sites in pairs oriented tandemly), we further calculated RAD21 reads normalized by how many times each barrier appeared at its genomic position (RAD21/CTCF). This normalization allowed us to measure RAD21 accumulation specific to each individual barrier. Specifically, we identified pairs of tandemly oriented barriers, and compared the relative enrichment of extruders between them by computing the ratio of extruder accumulation in the first versus the second barrier,

stratified by their spacing. Then we computed the cumulative distribution functions over their spacing separately for right-oriented and left-oriented barriers (Extended Data Fig. 11B). Finally, we assessed how extruder accumulation (for all orientations) scales with barrier proximity by comparing extruders versus barriers read counts across random configurations. We binned barriers by their nearest-neighbor distance and calculated the average extruder/barrier ratio in each bin (Extended Data Fig. 11A).

3D polymer simulations

We performed 3D polymer simulations for the targeted loading scenarios by modeling a 2.5 Mb segment of chromatin as a 50 nm polymer fiber, with each monomer corresponding to 2.5 kb of genomic DNA or 10 sites in the corresponding 1D lattice model. To implement the 3D polymer simulations, we used the Polychrom framework (https://github.com/open2c/polychrom), which leverages OpenMM[111] to simulate large ensembles of chromatin conformations. To simulate loop extrusion, we performed 200 3D steps between each 1D lattice update. Based on previous timescale matching[45], each simulated time step in 3D represents $\delta t_{3d} = 0.015$ sec to give a mean extruder residence time on chromatin of approximately 33 minutes. Loop extrusion was modeled by introducing harmonic bonds between the two monomers representing the arms of each extruder (positions *I* and *j*). As the loop extrusion factor progressed, these bonds were dynamically updated; removing the bond between *(I, j)* and adding a new bond between *(i–1, j+1)* to reflect loop enlargement. Under wild-type conditions, the polymer exhibited Rouse dynamics.

In silico Hi-C analysis

For in silico Hi-C analysis, we generated 3,000,000 polymer conformations from our 3D simulations for every parameter set we considered. Using these conformations, we constructed Hi-C contact maps at a resolution corresponding to the size of one monomer (2.5 kb), applying the default *polychrom* (https://github.com/open2c/polychrom) capture radius of 2.3 monomers to define contact events. This threshold closely matches empirical contact distance estimates[112]. Simulated contact matrices were converted into .cool format using *polykit* (https://github.com/open2c/polykit), facilitating analysis within the standard Hi-C data processing framework[113,114].

Code

Code specifying simulations and for performing analysis are available at: https://github.com/Fudenberg-Research-Group/Targeted_Cohesin_Loading

Determining the fraction of cohesin reads at CTCF sites

To measure the fraction of cohesin reads at CTCF sites, we first performed calibrated ChIP-seq with RAD21 (abcam ab154769) and SMC1 (Bethyl A300-055A) antibodies in untagged (E14) cells, untreated RAD21-eGFP-AID (EN272.2) cells, and EN272.2 cells in which RAD21 was degraded by adding 500 mM of Indole-3-Acetic Acid sodium salt (IAA, auxin analog, Tocris Bioscience 7932) to the culture media for 3.5 hours. The position of the degron tag precluded use of the Abcam ab992 RAD21 antibody used in other experiments. For each of two replicates, the number of cohesin reads in CTCF peaks was computed as in https://github.com/Fudenberg-Research-Group/fastaFRiP using deeptools.countReadsPerBin and then multiplied by the scaling factor. The background-corrected total number of reads was

calculated by (total mouse reads * scaling factor) – (total reads after RAD21 depletion * scaling factor). Finally, the corrected fraction of reads in CTCF peaks was calculated by (cohesin reads in CTCF peaks) / (background-corrected total reads).

Analysis of cohesin/CTCF ratios

We performed four replicates of calibrated ChIP-seq with CTCF (Active motif catalog number 61311) and RAD21 (Abcam ab992) antibodies in E14 ESCs. In NPCs, we performed two replicates each of CTCF and RAD21 ChIP-seq. For each protein, we combined equal numbers of reads from each of the ChIP-seq replicates. Approximately 46 million total reads were included for CTCF and RAD21 in ESC. For NPC analysis, the number of reads was normalized to match the number in ESCs. We used bedtools window to calculate the number of reads in each CTCF peak.

To calculate correlations in the number of reads in CTCF sites between ChIP-seq datasets, we used multiBigwigSummary and plotCorrelation from deeptools with the Pearson correlation method.

For comparing cohesin/CTCF ratios to the distance to the nearest enhancer, we used the enhancer list from[39]. For transcription start sites, we used transcript coordinates from GENCODE VM23 and included protein-coding genes with at least 1 transcript per million. Gene expression levels are from ENCODE RNA-seq in E14 mouse ESCs (identifier ENCSR000CWC)[115]. A and B compartments were called using the compartment_score function in GENOVA[116] with Hi-C data from two combined replicates of wild-type mESCs[23].

For the analysis of CTCF motif variants (Extended Data Fig. 6F), we used core, forward, and reverse motifs from[53]. We used FIMO from the MEME suite[117] to identify instances of the motifs ($p < 0.0001$) in the CTCF peaks. We plotted the RAD21/CTCF ratios for peaks in the following categories: only core motifs; at least one core and at least one upstream motif but no downstream motif; at least one core and at least one downstream motif but no upstream motif; no core motifs.

For analysis the of the distance over which CTCF sites can block cohesin traffic, we counted the number of forward and reverse core CTCF motifs[53] in each CTCF peak. We selected pairs of peaks that each contained only forward motifs and for which the next downstream peak was over 100 kb away, and similarly selected pairs of peaks with reverse motifs. For each pair, we calculated $\log_2$[(first peak RAD21/CTCF)/(second peak RAD21/CTCF)] and plotted the cumulative distribution of this metric based on the distance between the peaks.

Micro-C analysis

We analyzed micro-C from[118], using data with two pooled replicates from untreated mESCs (GSE178982_CTCF-UT_pool.mcool) or cells with 3 hours of CTCF depletion (GSE178982_CTCF-AID_pool.mcool). Plots show data normalized by the expected interaction frequencies. We ranked MAU2 peaks based on the number of ChIP-seq reads, and generated a pileup at the top one third of sites using cooltools.pileup[114]. Control sites were selected using bedtools shuffle[119] to choose random sites within TADs that contain a top MAU2 site, with TAD definitions from[118]. Repeated permutations of random sites yielded consistent pile-up plots.

Enformer

As Enformer is not trained on relevant mouse ESC datasets, we generated predictions for cohesin and CTCF binding in mouse CH12 cells. We downloaded CH12 CTCF and RAD21

ChIP-seq data from the ENCODE portal (identifiers ENCSR000ERM and ENCSR000ERK), mapped the reads as above, and called peaks using macs2. We selected a CTCF peak with a low RAD21/CTCF ratio (chr15:97665011-97665743) to use as a recipient locus, and selected ten CTCF peaks with higher CTCF/cohesin ratios to use as donor sequences. We then generated test sequences by swapping 512 bp (centered at the center of the CTCF peak) from the donor sequence into the recipient sequence. We used Enformer[120] to predict CH12 RAD21 and CTCF binding at the test sequences. We plotted the sum of the cohesin signal across the 512 bp divided by the sum of the CTCF signal across the 512 bp. We then modified the recipient sequence by replacing the CTCF motifs in the CTCF peaks flanking the central peak with neutral sequence (replacing 17 bp at each of four motifs), and repeated the swapping of the donor sequences into the modified recipient sequence.

Acknowledgements
We are grateful to members of Daniele Canzio's group for discussion and access to equipment, and to Alex Buckley, Simon Gaudin, Fernanda Vargas-Romero, Elzo de Wit, and Luca Giorgetti for critical feedback on the manuscript. We thank David Spector and Stanley Qi for the U2OS 2-6-3 cell line. Funding sources: Grant NIH R35GM142792 to EN, Grant NIH R35GM143116 to GF, the Chan-Zuckerberg Biohub San Francisco Investigator program to EN, the Sandler Program for Breakthrough Biomedical Research at UCSF, NSF EAGER grant 2313792 to EN, NIH training grant T32HL007731 (ECA), fellowships from the Helen Hay Whitney foundation (ECA), the UCSF-California Institute for Regenerative Medicine Scholars Training Program education grant EDUC4-12812 (ECA and KH), and KAUST Ibn Rushd Fellowship (AA). Part of the sequencing was performed at the UCSF CAT, supported by UCSF PBBR, RRP IMIA, and NIH 1S10OD028511-01 grants. Flow cytometry was performed in the Laboratory for Cell Analysis in the UCSF Helen Diller Family Comprehensive Cancer Center, supported by grant P30CA082103.

Author contributions
ECA performed, analyzed, or supervised all experiments except ORCA, with technical support from EMA, ASA, RS, KH, and EPN. HR performed simulations under the supervision of GF. AA designed, performed and analyzed ORCA with support from IC and under the supervision of ANB. EP designed the study with ECA and input from GF. ECA assembled figures and wrote the manuscript with assistance from EPN, GF, and input from all co-authors.

Ethics declaration
No competing interests to declare.

Data availability
Sequencing data was deposited to GEO GSE278338.

Code availability
https://github.com/hrahmanin/Target_cohesin_loading

1103 **References**

1104 1. Papantonis, A. & Oudelaar, A. M. Mechanisms of Enhancer-Mediated Gene Activation in the
1105 Context of the 3D Genome. *Annual Review of Genomics and Human Genetics* **26**, 163–188 (2025).
1106 2. Yang, J. H. & Hansen, A. S. Enhancer selectivity in space and time: from enhancer–promoter
1107 interactions to promoter activation. *Nat Rev Mol Cell Biol* **25**, 574–591 (2024).
1108 3. Davidson, I. F. & Peters, J.-M. Genome folding through loop extrusion by SMC complexes. *Nat Rev*
1109 *Mol Cell Biol* **22**, 445–464 (2021).
1110 4. de Wit, E. & Nora, E. P. New insights into genome folding by loop extrusion from inducible degron
1111 technologies. *Nat Rev Genet* **24**, 73–85 (2023).
1112 5. Allyn, B. M. *et al.* Promoter- and enhancer-dependent cohesin loading initiates chromosome
1113 looping to fold *Tcrb* loci for long-range recombination. *Cell Reports* **44**, 116133 (2025).
1114 6. Hua, P. *et al.* Defining genome architecture at base-pair resolution. *Nature* **595**, 125–129 (2021).
1115 7. Rinaldi, L. *et al.* The glucocorticoid receptor associates with the cohesin loader NIPBL to promote
1116 long-range gene regulation. *Science Advances* **8**, eabj8360 (2022).
1117 8. Rinzema, N. J. *et al.* Building regulatory landscapes reveals that an enhancer can recruit cohesin to
1118 create contact domains, engage CTCF sites and activate distant genes. *Nat Struct Mol Biol* **29**, 563–
1119 574 (2022).
1120 9. Valton, A.-L. *et al.* A cohesin traffic pattern genetically linked to gene regulation. *Nat Struct Mol*
1121 *Biol* **29**, 1239–1251 (2022).
1122 10. Vian, L. *et al.* The Energetics and Physiological Impact of Cohesin Extrusion. *Cell* **173**, 1165-
1123 1178.e20 (2018).
1124 11. Vos, E. S. M. *et al.* Interplay between CTCF boundaries and a super enhancer controls cohesin
1125 extrusion trajectories and gene expression. *Molecular Cell* **81**, 3082-3095.e6 (2021).
1126 12. Zhang, S., Übelmesser, N., Barbieri, M. & Papantonis, A. Enhancer–promoter contact formation
1127 requires RNAPII and antagonizes loop extrusion. *Nat Genet* **55**, 832–840 (2023).

1128 13. Barrington, C. *et al.* Enhancer accessibility and CTCF occupancy underlie asymmetric TAD
1129 architecture and cell type specific genome topology. *Nat Commun* **10**, 2908 (2019).
1130 14. Dorsett, D. & Merkenschlager, M. Cohesin at active genes: a unifying theme for cohesin and gene
1131 expression from model organisms to humans. *Current Opinion in Cell Biology* **25**, 327–333 (2013).
1132 15. Kagey, M. H. *et al.* Mediator and cohesin connect gene expression and chromatin architecture.
1133 *Nature* **467**, 430–435 (2010).
1134 16. Nitzsche, A. *et al.* RAD21 Cooperates with Pluripotency Transcription Factors in the Maintenance
1135 of Embryonic Stem Cell Identity. *PLOS ONE* **6**, e19470 (2011).
1136 17. Schmidt, D. *et al.* A CTCF-independent role for cohesin in tissue-specific transcription. *Genome*
1137 *Res.* **20**, 578–588 (2010).
1138 18. Selivanovskiy, A. V., Molodova, M. N., Khrameeva, E. E., Ulianov, S. V. & Razin, S. V. Liquid
1139 condensates: a new barrier to loop extrusion? *Cell. Mol. Life Sci.* **82**, 80 (2025).
1140 19. Ciosk, R. *et al.* Cohesin's Binding to Chromosomes Depends on a Separate Complex Consisting of
1141 Scc2 and Scc4 Proteins. *Molecular Cell* **5**, 243–254 (2000).
1142 20. Murayama, Y. & Uhlmann, F. Biochemical reconstitution of topological DNA binding by the
1143 cohesin ring. *Nature* **505**, 367–371 (2014).
1144 21. Davidson, I. F. *et al.* DNA loop extrusion by human cohesin. *Science* **366**, 1338–1345 (2019).
1145 22. Kim, Y., Shi, Z., Zhang, H., Finkelstein, I. J. & Yu, H. Human cohesin compacts DNA by loop
1146 extrusion. *Science* **366**, 1345–1349 (2019).
1147 23. Shah, R. *et al.* Dosage sensitivity of the loop extrusion rate confers tunability to genome folding
1148 while creating vulnerability to genetic disruption. 2025.08.14.667581 Preprint at
1149 https://doi.org/10.1101/2025.08.14.667581 (2025).
1150 24. Wutz, G. *et al.* PDS5 proteins control genome architecture by limiting the lifetime of cohesin-
1151 NIPBL complexes. 2025.08.30.673243 Preprint at https://doi.org/10.1101/2025.08.30.673243
1152 (2025).

1153 25. Galitsyna, A. *et al.* Extrusion fountains are hallmarks of chromosome organization emerging upon
1154 zygotic genome activation. 2023.07.15.549120 Preprint at
1155 https://doi.org/10.1101/2023.07.15.549120 (2023).
1156 26. Guo, Y. *et al.* Chromatin jets define the properties of cohesin-driven in vivo loop extrusion.
1157 *Molecular Cell* https://doi.org/10.1016/j.molcel.2022.09.003 (2022)
1158 doi:10.1016/j.molcel.2022.09.003.
1159 27. Kim, J., Wang, H. & Ercan, S. Cohesin organizes 3D DNA contacts surrounding active enhancers in
1160 C. elegans. *Genome Res* **35**, 1108–1123 (2025).
1161 28. Kraft, K. *et al.* Serial genomic inversions induce tissue-specific architectural stripes, gene
1162 misexpression and congenital malformations. *Nature Cell Biology* **21**, 305–310 (2019).
1163 29. Liu, N. Q. *et al.* Extrusion fountains are restricted by WAPL-dependent cohesin release and CTCF
1164 barriers. *Nucleic Acids Res* **53**, gkaf549 (2025).
1165 30. Lüthi, B. N. *et al.* Cohesin forms fountains at active enhancers in C. elegans. *Nat Commun*
1166 https://doi.org/10.1038/s41467-025-67302-6 (2025) doi:10.1038/s41467-025-67302-6.
1167 31. Banigan, E. J. *et al.* Transcription shapes 3D chromatin organization by interacting with loop
1168 extrusion. *Proceedings of the National Academy of Sciences* **120**, e2210480120 (2023).
1169 32. Chen, L.-F. *et al.* Structural elements promote architectural stripe formation and facilitate ultra-long-
1170 range gene regulation at a human disease locus. *Molecular Cell* **83**, 1446-1461.e6 (2023).
1171 33. Ollikainen, N., Ma, F., Braikia, F. Z. & Sen, R. Chromatin folding principles underlying the
1172 generation of antibody diversity. *Molecular Cell* https://doi.org/10.1016/j.molcel.2025.12.023
1173 (2026) doi:10.1016/j.molcel.2025.12.023.
1174 34. Bahr, C. *et al.* A Myc enhancer cluster regulates normal and leukaemic haematopoietic stem cell
1175 hierarchies. *Nature* **553**, 515–520 (2018).
1176 35. Kragesteen, B. K. *et al.* Dynamic 3D chromatin architecture contributes to enhancer specificity and
1177 limb morphogenesis. *Nat Genet* **50**, 1463–1473 (2018).

1178 36. Long, H. K. *et al.* Loss of Extreme Long-Range Enhancers in Human Neural Crest Drives a
1179 Craniofacial Disorder. *Cell Stem Cell* **27**, 765-783.e14 (2020).
1180 37. Spracklin, G. *et al.* Diverse silent chromatin states modulate genome compartmentalization and loop
1181 extrusion barriers. *Nat Struct Mol Biol* **30**, 38–51 (2023).
1182 38. Zuin, J. *et al.* A Cohesin-Independent Role for NIPBL at Promoters Provides Insights in CdLS.
1183 *PLOS Genetics* **10**, e1004153 (2014).
1184 39. Whyte, W. A. *et al.* Master Transcription Factors and Mediator Establish Super-Enhancers at Key
1185 Cell Identity Genes. *Cell* **153**, 307–319 (2013).
1186 40. Janicki, S. M. *et al.* From Silencing to Gene Expression: Real-Time Analysis in Single Cells. *Cell*
1187 **116**, 683–698 (2004).
1188 41. Han, R. *et al.* Characterization of induced cohesin loop extrusion trajectories in living cells. *Nat*
1189 *Genet* **57**, 2785–2797 (2025).
1190 42. Hansen, K. L. *et al.* Synergy between regulatory elements can render cohesin dispensable for distal
1191 enhancer function. *Science* **0**, eadt4221 (2025).
1192 43. Rekaik, H. *et al.* Sequential and directional insulation by conserved CTCF sites underlies the Hox
1193 timer in stembryos. *Nat Genet* **55**, 1164–1175 (2023).
1194 44. Fudenberg, G. *et al.* Formation of Chromosomal Domains by Loop Extrusion. *Cell Reports* **15**,
1195 2038–2049 (2016).
1196 45. Rahmaninejad, H., Xiao, Y., Tortora, M. M. C. & Fudenberg, G. Dynamic barriers modulate cohesin
1197 positioning and genome folding at fixed occupancy. *Genome Res.*
1198 https://doi.org/10.1101/gr.280108.124 (2025) doi:10.1101/gr.280108.124.
1199 46. Parelho, V. *et al.* Cohesins Functionally Associate with CTCF on Mammalian Chromosome Arms.
1200 *Cell* **132**, 422–433 (2008).
1201 47. Rubio, E. D. *et al.* CTCF physically links cohesin to chromatin. *Proceedings of the National*
1202 *Academy of Sciences* **105**, 8309–8314 (2008).

1203 48. Wendt, K. S. *et al.* Cohesin mediates transcriptional insulation by CCCTC-binding factor. *Nature*
1204 **451**, 796–801 (2008).
1205 49. Hu, B. *et al.* Biological chromodynamics: a general method for measuring protein occupancy across
1206 the genome by calibrating ChIP-seq. *Nucleic Acids Res* **43**, e132–e132 (2015).
1207 50. Hafner, A. *et al.* Loop stacking organizes genome folding from TADs to chromosomes. *Molecular*
1208 *Cell* **83**, 1377-1392.e6 (2023).
1209 51. Liu, N. Q. *et al.* WAPL maintains a cohesin loading cycle to preserve cell-type-specific distal gene
1210 regulation. *Nature Genetics* **53**, 100–109 (2021).
1211 52. Szabo, Q. *et al.* Regulation of single-cell genome organization into TADs and chromatin
1212 nanodomains. *Nat Genet* **52**, 1151–1157 (2020).
1213 53. Nakahashi, H. *et al.* A Genome-wide Map of CTCF Multivalency Redefines the CTCF Code. *Cell*
1214 *Reports* **3**, 1678–1689 (2013).
1215 54. Busslinger, G. A. *et al.* Cohesin is positioned in mammalian genomes by transcription, CTCF and
1216 Wapl. *Nature* **544**, 503–507 (2017).
1217 55. Chapard, C. *et al.* RNA Pol II-based regulations of chromosome folding. *Cell Genomics* 100970
1218 (2025) doi:10.1016/j.xgen.2025.100970.
1219 56. Heinz, S. *et al.* Transcription Elongation Can Affect Genome 3D Structure. *Cell* **174**, 1522-1536.e22
1220 (2018).
1221 57. Zuin, J. *et al.* Nonlinear control of transcription through enhancer–promoter interactions. *Nature*
1222 **604**, 571–577 (2022).
1223 58. Kubo, N. *et al.* Promoter-proximal CTCF binding promotes distal enhancer-dependent gene
1224 activation. *Nat Struct Mol Biol* **28**, 152–161 (2021).
1225 59. Barth, R. *et al.* SMC motor proteins extrude DNA asymmetrically and can switch directions. *Cell*
1226 **188**, 749-763.e21 (2025).
1227 60. Georgiades, E. *et al.* Active regulatory elements recruit cohesin to establish cell specific chromatin
1228 domains. *Sci Rep* **15**, 11780 (2025).

1229 61. Schmitt, A. D. *et al.* A Compendium of Chromatin Contact Maps Reveals Spatially Active Regions
1230 in the Human Genome. *Cell Reports* **17**, 2042–2059 (2016).
1231 62. Rao, S. S. P. *et al.* Cohesin Loss Eliminates All Loop Domains. *Cell* **171**, 305-320.e24 (2017).
1232 63. Muñoz, S., Minamino, M., Casas-Delucchi, C. S., Patel, H. & Uhlmann, F. A Role for Chromatin
1233 Remodeling in Cohesin Loading onto Chromosomes. *Molecular Cell* **74**, 664-673.e5 (2019).
1234 64. Efroni, S. *et al.* Global Transcription in Pluripotent Embryonic Stem Cells. *Cell Stem Cell* **2**, 437–
1235 447 (2008).
1236 65. Ubertini, M. *et al.* Loop extrusion creates rare, long-lived encounters underlying enhancer-promoter
1237 communication. 2025.09.24.678119 Preprint at https://doi.org/10.1101/2025.09.24.678119 (2025).
1238 66. Cuadrado, A. *et al.* Contribution of variant subunits and associated factors to genome-wide
1239 distribution and dynamics of cohesin. *Epigenetics & Chromatin* **15**, 37 (2022).
1240 67. van den Berg, D. L. C. *et al.* Nipbl Interacts with Zfp609 and the Integrator Complex to Regulate
1241 Cortical Neuron Migration. *Neuron* **93**, 348–361 (2017).
1242 68. Zhu, Y., Denholtz, M., Lu, H. & Murre, C. Calcium signaling instructs NIPBL recruitment at active
1243 enhancers and promoters via distinct mechanisms to reconstruct genome compartmentalization.
1244 *Genes Dev.* https://doi.org/10.1101/gad.343475.120 (2020) doi:10.1101/gad.343475.120.
1245 69. Chen, X. *et al.* Integration of External Signaling Pathways with the Core Transcriptional Network in
1246 Embryonic Stem Cells. *Cell* **133**, 1106–1117 (2008).
1247 70. Fettweis, G. *et al.* Transcription factors form a ternary complex with NIPBL/MAU2 to localize
1248 cohesin at enhancers. *Nucleic Acids Res* **53**, gkaf415 (2025).
1249 71. Mattingly, M. *et al.* Mediator recruits the cohesin loader Scc2 to RNA Pol II-transcribed genes and
1250 promotes sister chromatid cohesion. *Current Biology* **32**, 2884-2896.e6 (2022).
1251 72. Linares-Saldana, R. *et al.* BRD4 orchestrates genome folding to promote neural crest differentiation.
1252 *Nat Genet* **53**, 1480–1492 (2021).

1253 73. Tei, S. *et al.* Cohesin acts as a transcriptional gatekeeper by restraining pause–release to promote
1254 processive elongation. 2025.09.30.679672 Preprint at https://doi.org/10.1101/2025.09.30.679672
1255 (2025).
1256 74. Bryan, A. F., Justice, M., Stutzman, A. V., McKay, D. J. & Dowen, J. M. Cohesin stabilization at
1257 promoters and enhancers by common transcription factors and chromatin regulators. *Epigenetics &*
1258 *Chromatin* **18**, 33 (2025).
1259 75. Cuadrado, A. *et al.* Specific Contributions of Cohesin-SA1 and Cohesin-SA2 to TADs and
1260 Polycomb Domains in Embryonic Stem Cells. *Cell Reports* **27**, 3500-3510.e4 (2019).
1261 76. Grant, Z. L. *et al.* Dose-dependent sensitivity of human 3D chromatin to a heart disease-linked
1262 transcription factor. 2025.01.09.632202 Preprint at https://doi.org/10.1101/2025.01.09.632202
1263 (2025).
1264 77. Zhou, Y. *et al.* Lineage-determining transcription factors constrain cohesin to drive multi-enhancer
1265 oncogene regulation. *Nat Cell Biol* 1–17 (2025) doi:10.1038/s41556-025-01827-2.
1266 78. Platania, A. *et al.* Competition between transcription and loop extrusion modulates promoter and
1267 enhancer dynamics. 2023.04.25.538222 Preprint at https://doi.org/10.1101/2023.04.25.538222
1268 (2023).
1269 79. Tang, W. *et al.* Cohesin positions the epigenetic reader Phf2 within the genome. *The EMBO Journal*
1270 **44**, 736–766 (2025).
1271 80. Nguyen, T. *et al.* Chromatin sequesters pioneer transcription factor Sox2 from exerting force on
1272 DNA. *Nat Commun* **13**, 3988 (2022).
1273 81. Davidson, I. F. *et al.* CTCF is a DNA-tension-dependent barrier to cohesin-mediated loop extrusion.
1274 *Nature* **616**, 822–827 (2023).
1275 82. Bintu, B. *et al.* Super-resolution chromatin tracing reveals domains and cooperative interactions in
1276 single cells. *Science* **362**, eaau1783 (2018).
1277 83. Gabriele, M. *et al.* Dynamics of CTCF- and cohesin-mediated chromatin looping revealed by live-
1278 cell imaging. *Science* https://doi.org/10.1126/science.abn6583 (2022) doi:10.1126/science.abn6583.

1279 84. Mach, P. *et al.* Cohesin and CTCF control the dynamics of chromosome folding. *Nat Genet* **54**,
1280 1907–1918 (2022).
1281 85. Sabaté, T. *et al.* Uniform dynamics of cohesin-mediated loop extrusion in living human cells. *Nat*
1282 *Genet* 1–13 (2025) doi:10.1038/s41588-025-02406-9.
1283 86. Smaruj, P. N., Kamulegeya, F., Kelley, D. R. & Fudenberg, G. Interpreting the CTCF-mediated
1284 sequence grammar of genome folding with AkitaV2. *PLOS Computational Biology* **21**, e1012824
1285 (2025).
1286 87. Amândio, A. R. *et al.* Sequential in cis mutagenesis in vivo reveals various functions for CTCF sites
1287 at the mouse HoxD cluster. *Genes Dev.* **35**, 1490–1509 (2021).
1288 88. Anania, C. *et al.* In vivo dissection of a clustered-CTCF domain boundary reveals developmental
1289 principles of regulatory insulation. *Nat Genet* **54**, 1026–1036 (2022).
1290 89. Despang, A. *et al.* Functional dissection of the Sox9–Kcnj2 locus identifies nonessential and
1291 instructive roles of TAD architecture. *Nat Genet* **51**, 1263–1271 (2019).
1292 90. Kiefer, L. *et al.* Tuning cohesin trajectories enables differential readout of the Pcdhα cluster across
1293 neurons. *Science* **385**, eadm9802 (2024).
1294 91. Kiefer, L. *et al.* WAPL functions as a rheostat of Protocadherin isoform diversity that controls neural
1295 wiring. *Science* **380**, eadf8440 (2023).
1296 92. Yang, J. H., Brandão, H. B. & Hansen, A. S. DNA double-strand break end synapsis by DNA loop
1297 extrusion. *Nat Commun* **14**, 1913 (2023).
1298 93. Meisenberg, C. *et al.* Repression of Transcription at DNA Breaks Requires Cohesin throughout
1299 Interphase and Prevents Genome Instability. *Mol Cell* **73**, 212-223.e7 (2019).
1300 94. Piveteau, V. *et al.* Condensin loop extrusion properties, roadblocks, and role in homology search in
1301 S. cerevisiae. 2024.09.12.612585 Preprint at https://doi.org/10.1101/2024.09.12.612585 (2026).
1302 95. Li, H. *et al.* The Sequence Alignment/Map format and SAMtools. *Bioinformatics* **25**, 2078–2079
1303 (2009).

1304 96. Ramírez, F. *et al.* deepTools2: a next generation web server for deep-sequencing data analysis.
1305 *Nucleic Acids Res* **44**, W160–W165 (2016).
1306 97. Fursova, N. A. *et al.* Synergy between Variant PRC1 Complexes Defines Polycomb-Mediated Gene
1307 Repression. *Molecular Cell* **74**, 1020-1036.e8 (2019).
1308 98. Perez, G. *et al.* The UCSC Genome Browser database: 2025 update. *Nucleic Acids Res* **53**, D1243–
1309 D1249 (2025).
1310 99. Zhang, Y. *et al.* Model-based Analysis of ChIP-Seq (MACS). *Genome Biology* **9**, R137 (2008).
1311 100. Amemiya, H. M., Kundaje, A. & Boyle, A. P. The ENCODE Blacklist: Identification of Problematic
1312 Regions of the Genome. *Sci Rep* **9**, 9354 (2019).
1313 101. Khan, A. & Mathelier, A. Intervene: a tool for intersection and visualization of multiple gene or
1314 genomic region sets. *BMC Bioinformatics* **18**, 287 (2017).
1315 102. Dubarry, M., Loïodice, I., Chen, C. L., Thermes, C. & Taddei, A. Tight protein–DNA interactions
1316 favor gene silencing. *Genes Dev.* **25**, 1365–1370 (2011).
1317 103. Gehring, J., Hwee Park, J., Chen, S., Thomson, M. & Pachter, L. Highly multiplexed single-cell
1318 RNA-seq by DNA oligonucleotide tagging of cellular proteins. *Nat Biotechnol* **38**, 35–38 (2020).
1319 104. Mateo, L. J. *et al.* Visualizing DNA folding and RNA in embryos at single-cell resolution. *Nature*
1320 **568**, 49–54 (2019).
1321 105. Mateo, L. J., Sinnott-Armstrong, N. & Boettiger, A. N. Tracing DNA paths and RNA profiles in
1322 cultured cells and tissues with ORCA. *Nat Protoc* **16**, 1647–1713 (2021).
1323 106. Rigano, A. *et al.* Micro-Meta App: an interactive tool for collecting microscopy metadata based on
1324 community specifications. *Nat Methods* **18**, 1489–1495 (2021).
1325 107. Stringer, C., Wang, T., Michaelos, M. & Pachitariu, M. Cellpose: a generalist algorithm for cellular
1326 segmentation. *Nat Methods* **18**, 100–106 (2021).
1327 108. Cattoglio, C. *et al.* Determining cellular CTCF and cohesin abundances to constrain 3D genome
1328 models. *eLife* **8**, e40164 (2019).

1329 109. Sönmezer, C. *et al.* Molecular Co-occupancy Identifies Transcription Factor Binding Cooperativity
1330 *In Vivo*. *Molecular Cell* **81**, 255-267.e6 (2021).
1331 110. Hansen, A. S., Pustova, I., Cattoglio, C., Tjian, R. & Darzacq, X. CTCF and cohesin regulate
1332 chromatin loop stability with distinct dynamics. *eLife* **6**, e25776 (2017).
1333 111. Eastman, P. *et al.* OpenMM 7: Rapid development of high performance algorithms for molecular
1334 dynamics. *PLOS Computational Biology* **13**, e1005659 (2017).
1335 112. McCord, R. P., Kaplan, N. & Giorgetti, L. Chromosome Conformation Capture and Beyond:
1336 Toward an Integrative View of Chromosome Structure and Function. *Molecular Cell* **77**, 688–708
1337 (2020).
1338 113. Abdennur, N. & Mirny, L. A. Cooler: scalable storage for Hi-C data and other genomically labeled
1339 arrays. *Bioinformatics* **36**, 311–316 (2020).
1340 114. Open2C *et al.* Cooltools: Enabling high-resolution Hi-C analysis in Python. *PLOS Computational*
1341 *Biology* **20**, e1012067 (2024).
1342 115. Dunham, I. *et al.* An integrated encyclopedia of DNA elements in the human genome. *Nature* **489**,
1343 57–74 (2012).
1344 116. van der Weide, R. H. *et al.* Hi-C analyses with GENOVA: a case study with cohesin variants. *NAR*
1345 *Genomics and Bioinformatics* **3**, lqab040 (2021).
1346 117. Grant, C. E., Bailey, T. L. & Noble, W. S. FIMO: scanning for occurrences of a given motif.
1347 *Bioinformatics* **27**, 1017–1018 (2011).
1348 118. Hsieh, T.-H. S. *et al.* Enhancer-promoter interactions and transcription are largely maintained upon
1349 acute loss of CTCF, cohesin, WAPL or YY1. *Nat Genet* **54**, 1919–1932 (2022).
1350 119. Quinlan, A. R. & Hall, I. M. BEDTools: a flexible suite of utilities for comparing genomic features.
1351 *Bioinformatics* **26**, 841–842 (2010).
1352 120. Avsec, Ž. *et al.* Effective gene expression prediction from sequence by integrating long-range
1353 interactions. *Nat Methods* **18**, 1196–1203 (2021).

1354 121. King, H. W. & Klose, R. J. The pioneer factor OCT4 requires the chromatin remodeller BRG1 to
1355 support gene regulatory element function in mouse embryonic stem cells. *eLife* **6**, e22631 (2017).

1356
1357

Figure 1

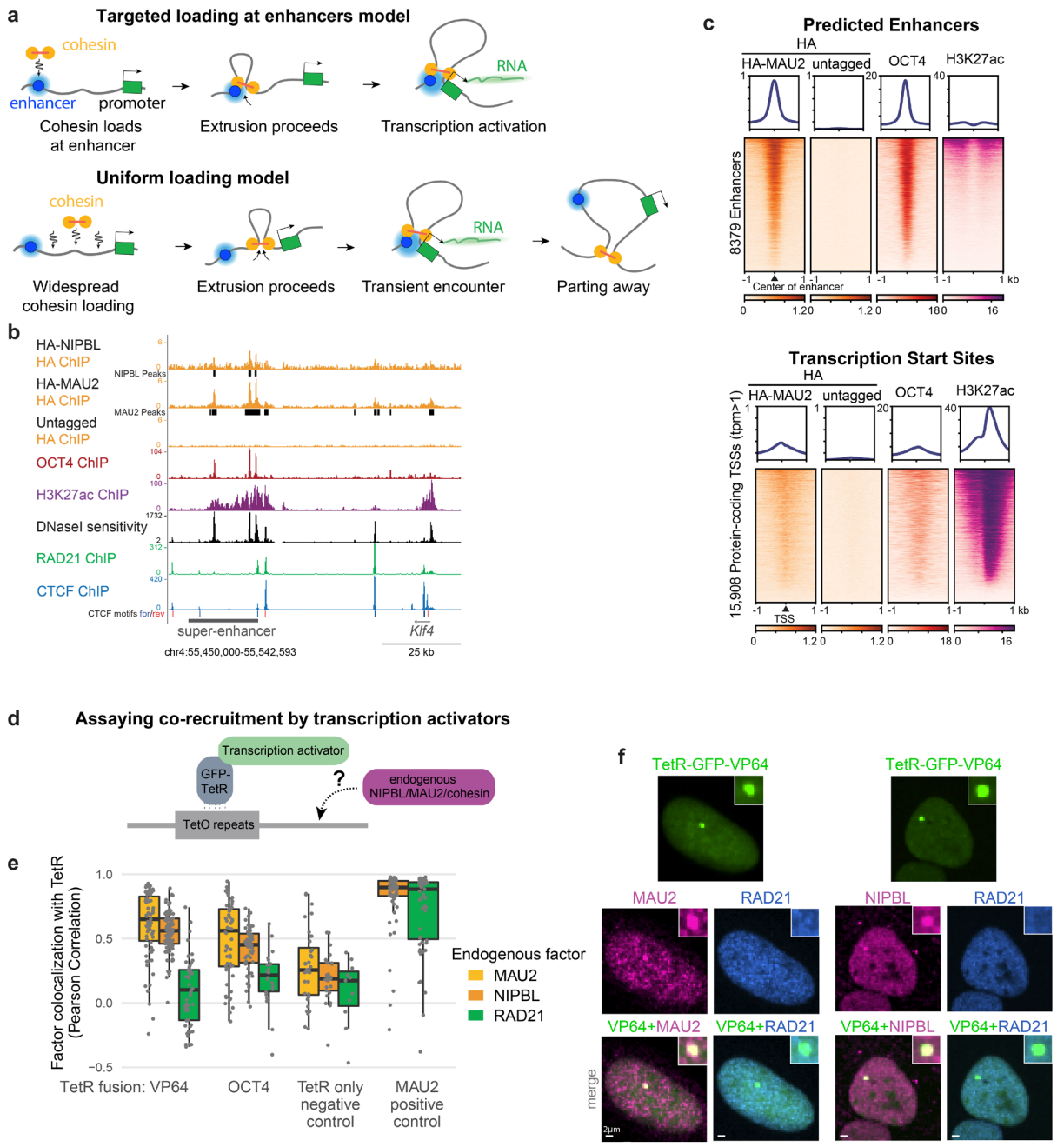

Figure 1: Enhancers bind NIPBL/MAU2 without strongly enriching cohesin
a, In the targeted loading model, cohesin is preferentially loaded at enhancers and extrudes toward target promoters to support long-range transcriptional activation. In contrast, in the uniform loading model most cohesin loads away from enhancers and bridges enhancers to their target promoters only transiently. **b**, ChIP-seq in tagged mouse embryonic stem cells (ESCs) shows high NIPBL/MAU2 binding at a distal enhancer, overlapping OCT4 binding sites, but not at a promoter. OCT4 ChIP-seq from ref[51] and DNAseI sensitivity from ref[115]. **c**, MAU2 ChIP

1366 signal is enriched at predicted pluripotency enhancers (from ref[39]) more than that at
1367 transcriptionally active TSSs. **d**, Experimental strategy to test co-recruitment of endogenous
1368 NIPBL, MAU2, and cohesin by transcriptional activators. TetR-GFP-fused transcription
1369 activators were expressed in U2OS cells with a large heterozygous TetO array[40] and endogenous
1370 NIPBL, MAU2, or cohesin were stained by immunofluorescence. **e**, Quantification of
1371 colocalization between TetR-GFP and NIPBL, MAU2, or cohesin at the TetO array. Each point
1372 denotes the Pearson correlation coefficient between the two proteins in a single cell. TetR-GFP
1373 fused to transcriptional activators (VP64 or OCT4) recruits MAU2 and NIPBL but not the
1374 cohesin subunit RAD21. TetR alone serves as a negative control, whereas TetR-MAU2 provides
1375 a positive control for cohesin recruitment. Boxes indicate interquartile range; center lines denote
1376 medians. **f**, Example cells showing that tethering VP64 recruits endogenous MAU2 and NIPBL
1377 but no detectable cohesin RAD21.

Figure 2

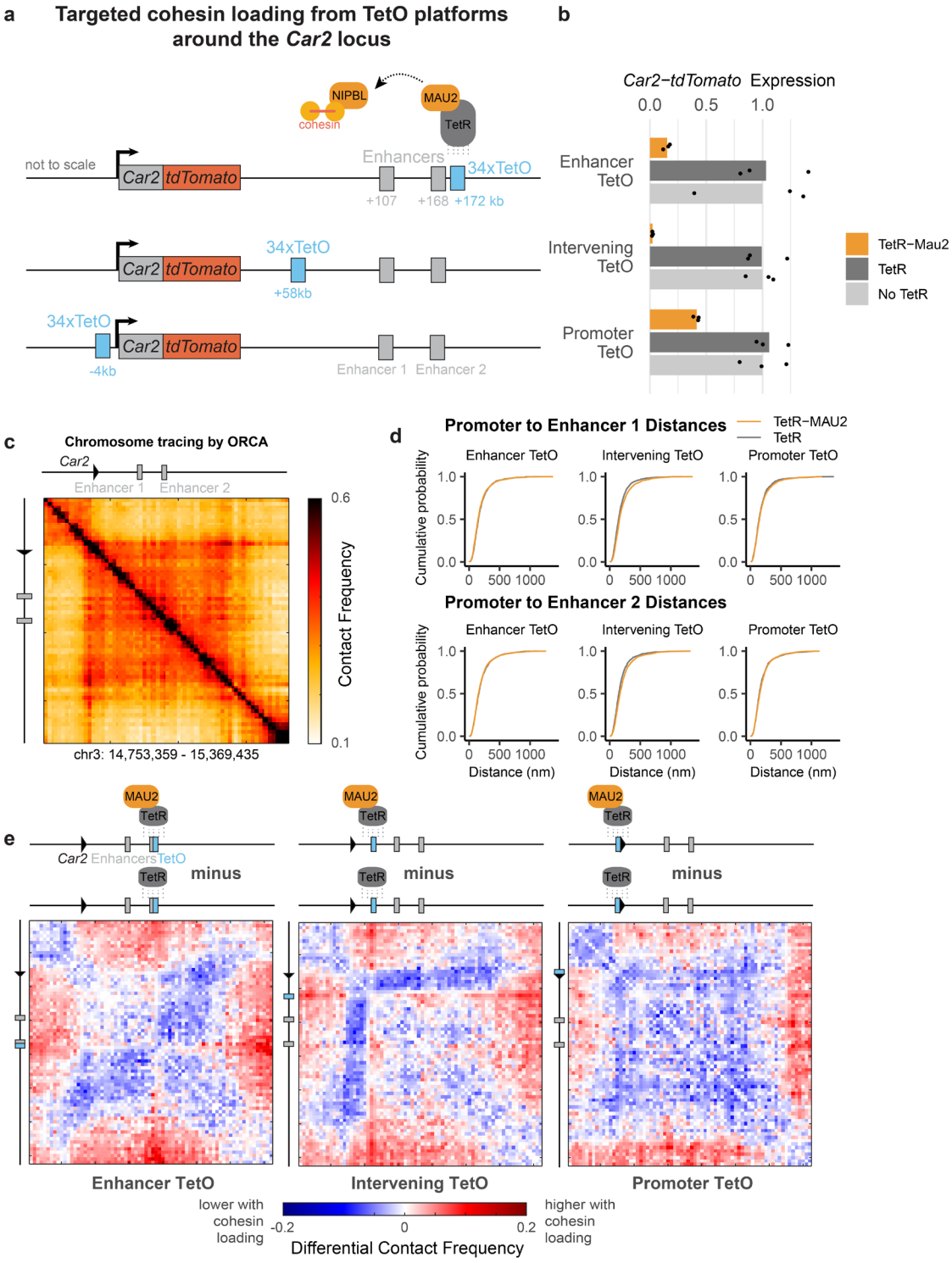

1378

1379 **Figure 2: Targeted cohesin recruitment interferes with transcription.**
1380 **a**, TetR-MAU2 was stably expressed to force cohesin loading at 34x TetO arrays (2 kb) inserted
1381 at three positions across the *Car2* locus in ESCs. **b**, *Car2* expression, measured by flow
1382 cytometry, was reduced by forcing cohesin loading at all tested positions, whereas TetR binding
1383 alone had no detectable effect. Values are normalized to corresponding parental cells. Points
1384 show three biological replicates from separate transfections of the respective TetR-expressing
1385 plasmid. **c**, DNA FISH chromosome tracing (ORCA) heatmap showing contact frequencies
1386 (within ~200 nm, see methods) at the *Car2* locus (8 kb resolution). **d**, Cumulative plots showing
1387 the distribution of 3D distances between the *Car2* promoter and each of its enhancers on the
1388 TetO allele with either TetR-MAU2 (forced cohesin loading) or TetR expression (control). **e**,
1389 Differential contact maps comparing TetR-MAU2 cells to TetR-only controls (comprising >1300
1390 traces per condition). Targeted cohesin loading does not increase enhancer-promoter interactions
1391 but instead creates a boundary, (except at the *Car2* promoter, which is located near an
1392 endogenous TAD boundary). The modest reduction in interactions across the TAD arises from
1393 global MAU2 overexpression rather than from targeted loading at the TetO site (see allele-
1394 specific comparisons within TetR-MAU2 cells in Extended Data Fig. 4B).

Figure 3

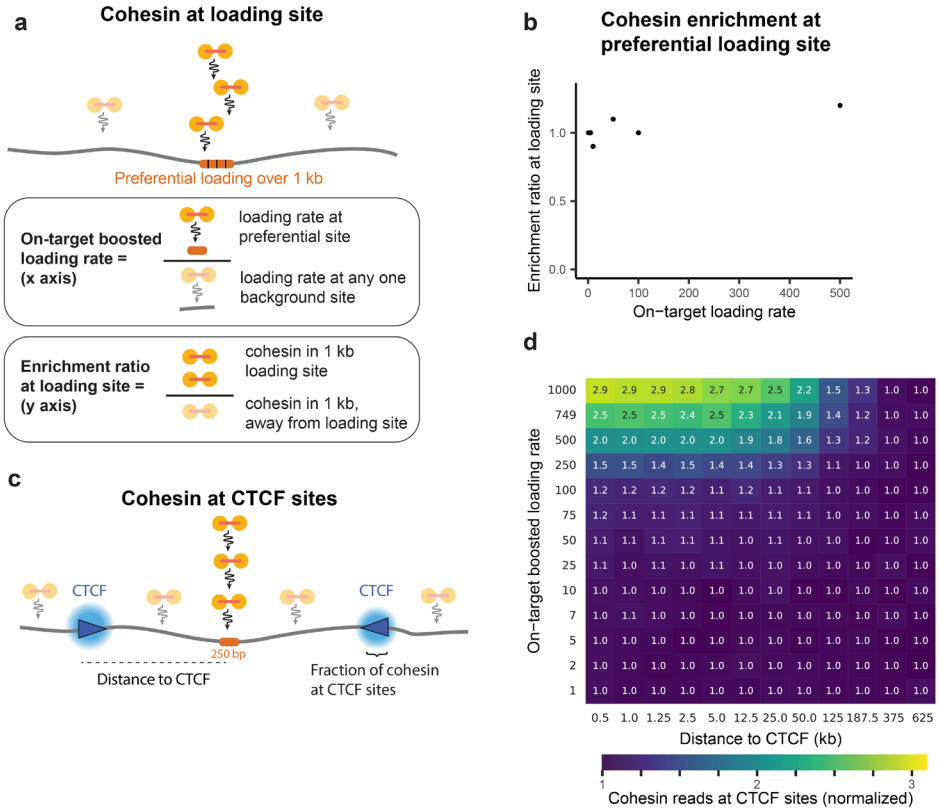

Figure 3: Simulations show minimal effect of targeted loading on cohesin traffic. **a**, and **b,** A 1D lattice simulation indicates that cohesin is not expected to accumulate at loading sites, even at high loading rates. The loading site is modeled as four adjacent monomers spanning 1 kb. The enrichment ratio is defined as the density of cohesin within a 1-kb window centered on the preferential loading site relative to background sites. **c**, Simulations exploring the effect of increasing loading rates at a single site on cohesin accumulation at neighboring CTCF sites (50% occupancy dynamic barrier, see Methods). Here, targeted loading rate at a single 250 bp monomer is increased while maintaining a constant loading rate at all other monomers. **d**, Number of cohesin reads at the CTCF site as a function of the on-target loading boost and the distance between the loading site and CTCF sites. As a reference, values are normalized to the condition with baseline loading rate (1x boost) and a CTCF site positioned 0.5 kb from the loading site.

Figure 4

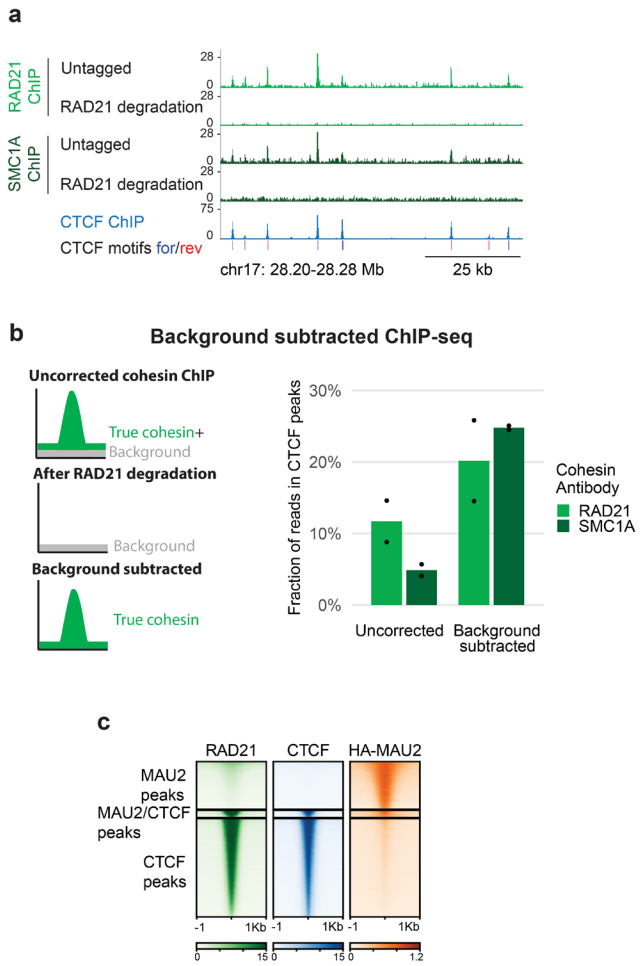

Figure 4: Cohesin binding is largely between CTCF sites

a, Spike-in calibrated ChIP-seq for cohesin subunits RAD21 and SMC1A in untagged ESCs or after cohesin degradation in RAD21-AID ESCs treated with auxin (IAA) for 3.5 hours. **b**, Strategy to calculate true cohesin binding by subtracting background antibody signal from the total reads. After background subtraction, CTCF peaks contain ~25% of cohesin ChIP-seq reads (average of two biological replicates). **c**, ChIP-seq shows little binding of the cohesin subunit RAD21 at NIPBL/MAU2 sites compared to CTCF sites.

Figure 5

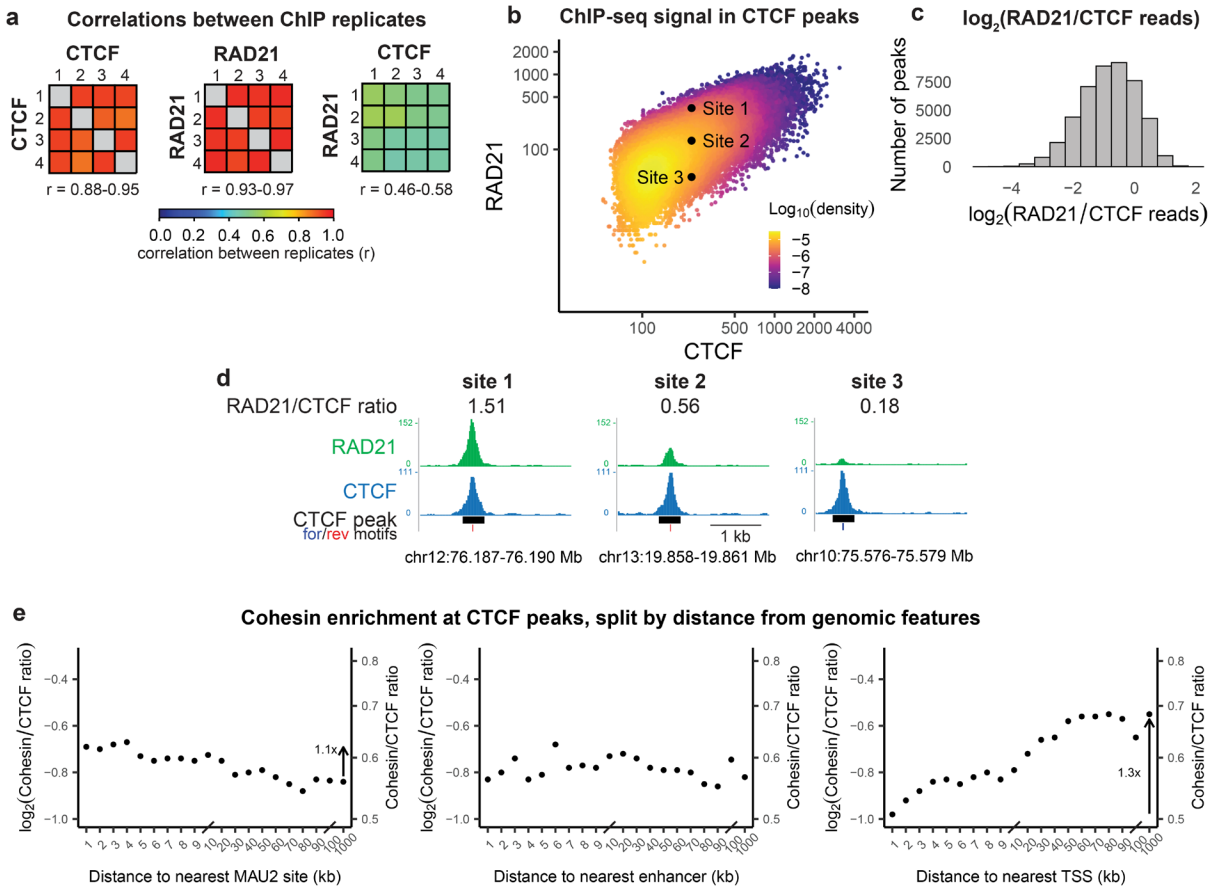

Figure 5: NIPBL/MAU2 binding sites have minimal effects on local cohesin levels. **a**, Correlation matrices (Pearson correlation coefficients) comparing ChIP–seq signal at CTCF sites across biological replicates for CTCF and RAD21, showing that replicates of the same factor correlate more strongly with each other than with the other factor. **b**, Scatter plot of RAD21 vs. CTCF reads in each CTCF peak (from four combined ChIP-seq replicates), highlighting substantial variability in cohesin occupancy at sites with similar CTCF binding. **c**, Distribution of RAD21/CTCF ratios. **d**, Example sites with the same CTCF occupancy but six-fold range in cohesin levels. **e**, Average cohesin/CTCF ratio as a function of the distance from the CTCF peak to the nearest MAU2 site, enhancer[39], or active TSS, showing minimal dependence on proximity to NIPBL/MAU2 binding and increased cohesin levels at greater distances from active TSSs.

Figure 6

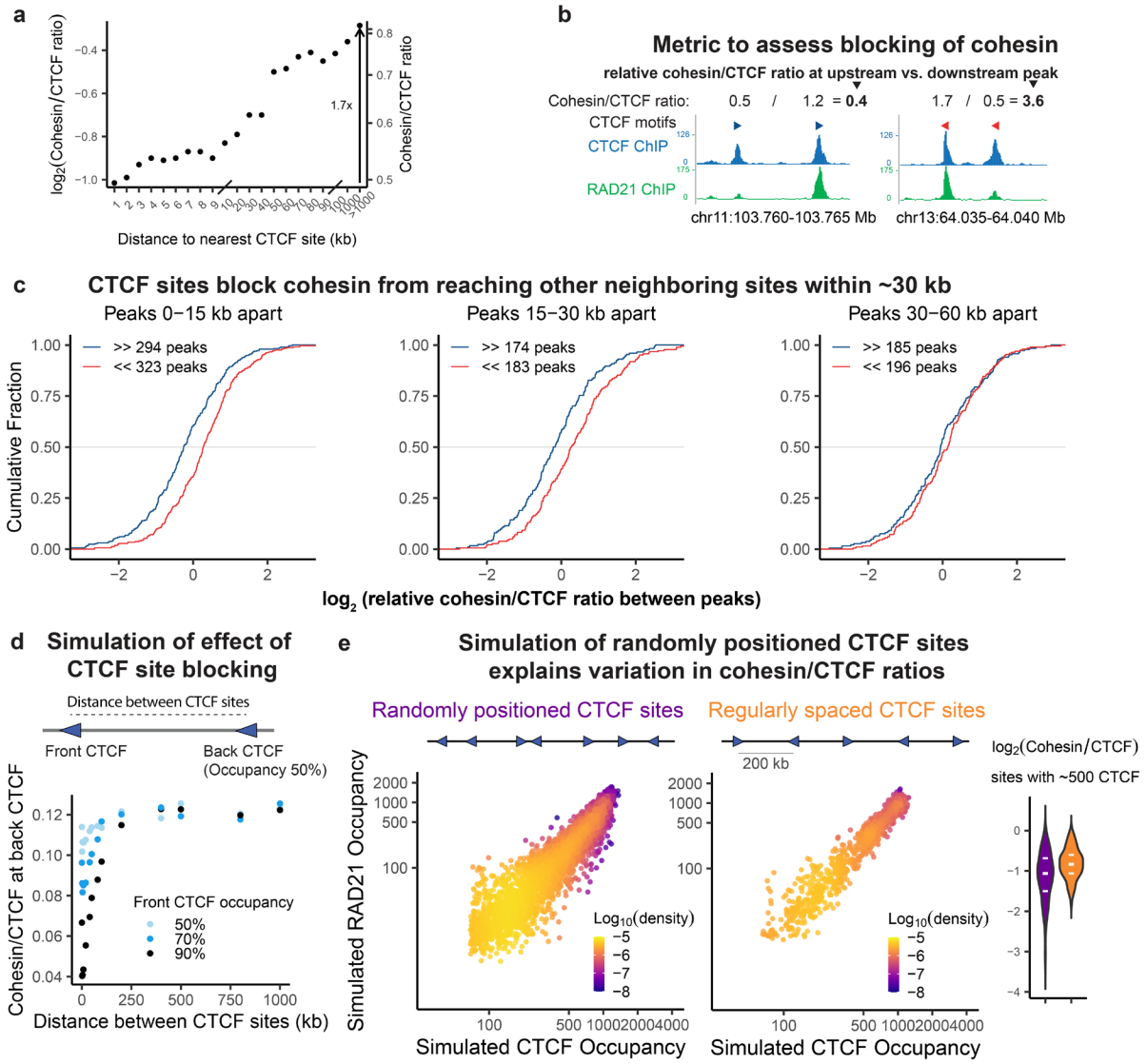

Figure 6: Clustered CTCF sites impede cohesin traffic.
a, Average cohesin/CTCF ratio at CTCF peaks as a function of distance to the nearest neighboring CTCF site, revealing reduced cohesin occupancy at closely spaced sites. **b**, We identified pairs of CTCF sites with forward motifs and where there is no other CTCF site within the downstream 100 kb. Relative cohesin/CTCF ratios compare upstream and downstream peaks based on motif orientation: a relative ratio less than 1 indicates that the rightmost peak is blocking cohesin from reaching the leftmost peak. For pairs of peaks with reverse motifs, a relative cohesin/CTCF ratio greater than 1 indicates blocking by the leftmost peak. **c**, Cumulative distributions of relative cohesin/CTCF ratios for CTCF site pairs with forward or reverse motifs, stratified by inter-site distance. Interference between neighboring CTCF sites is apparent only for sites within 30 kb of each other. **d**, In a simulation of two CTCF sites with reverse motifs, the cohesin/CTCF ratio at the rightmost site depends on the distance between sites and the occupancy of the left site. **e**, Cohesin vs. CTCF occupancy in a simulation of a 75 Mb

1443 chromosome with randomly positioned CTCF sites shows more dispersion than a simulation
1444 with CTCF sites regularly positioned every 200 kb. The CTCF occupancy is varied by altering
1445 the bound time while keeping the CTCF unbound time constant between sites.

Extended Data Figures

Extended Data Figure 1

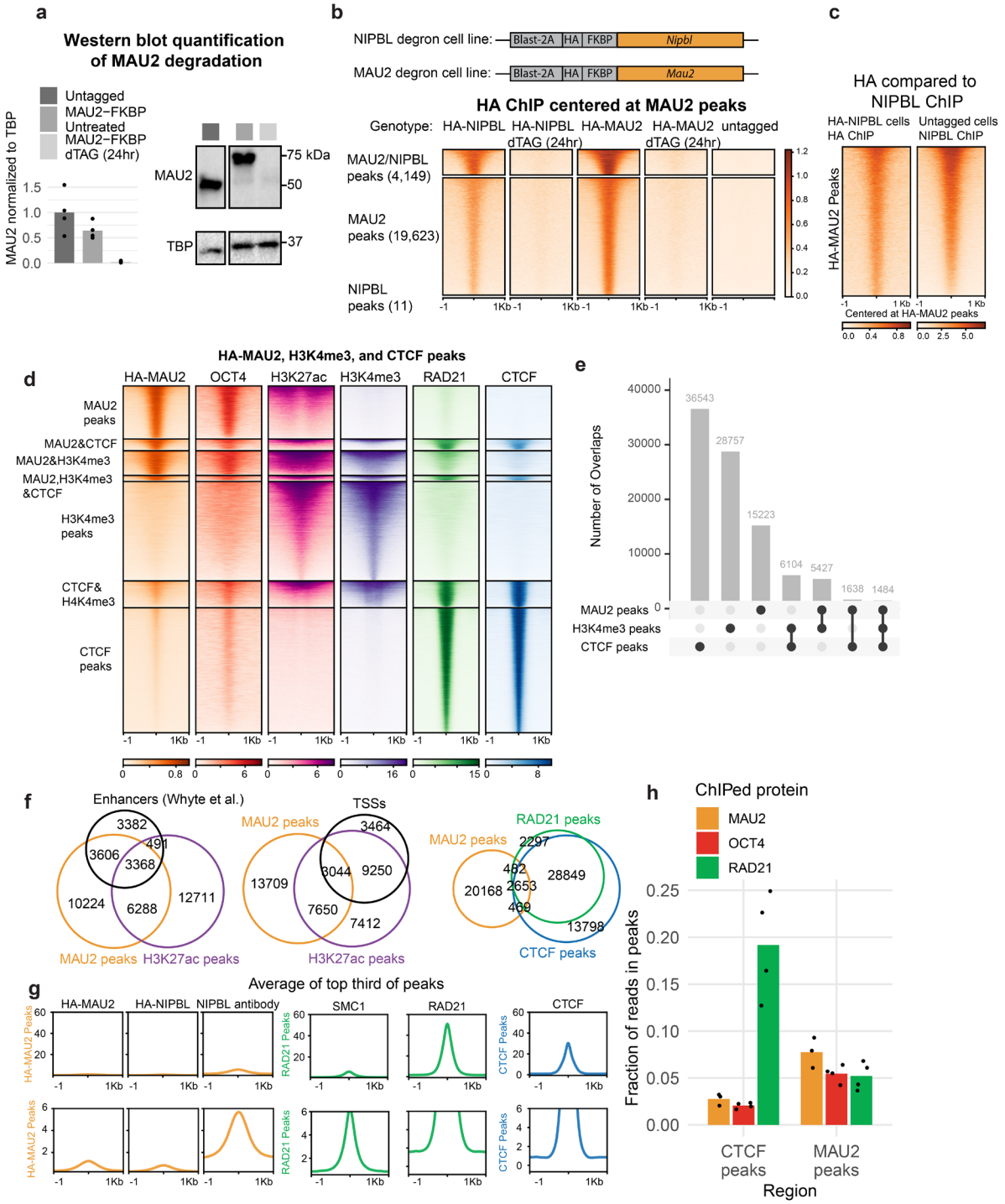

1448 **Extended Data Figure 1: Reproducible NIPBL/MAU2 binding sites overlap with enhancers**
1449 **in mouse ESCs.**
1450 **a,** Western blots show depletion of MAU2-FKBP after 24 hr dTAG treatment. **b**, HA ChIP-seq
1451 signal at MAU2 and NIPBL peaks is lost after NIPBL or MAU2 degradation (24 hr dTAG
1452 treatment). NIPBL and MAU2 co-bind the same sites, with the more sensitive HA-MAU2 ChIP-
1453 seq detecting more peaks. **c**, HA-NIPBL ChIP-seq signal closely matches ChIP-seq with an
1454 endogenous NIPBL antibody. **d**, Integration of ChIP-seq datasets highlighting that MAU2 binds
1455 the subset of active chromatin sites (H3K27ac) that bind OCT4 (enhancers). RAD21 (cohesin) is
1456 enriched at CTCF sites, with minimal signal at enhancers/MAU2 sites. OCT4 data is from ref[51]
1457 and H3K4me3 from ref[115]. **e**, Upset plot showing that MAU2, H3K4me3 (marking promoters),
1458 and CTCF largely bind distinct loci. **f**, Overlap of MAU2 peaks with active chromatin (H3K27ac
1459 peaks), enhancers (defined as sites bound by pluripotency transcription factors OCT4, SOX2,
1460 and NANOG from ref[39]), TSS regions (defined as 1 kb upstream of TSSs of GENCODE protein-
1461 coding genes expressed at >1 transcript per million), RAD21 peaks, and CTCF peaks. **g**, Average
1462 binding profiles of NIPBL/MAU2, cohesin subunits, and CTCF at their own peaks, showing that
1463 NIPBL/MAU2 binding sites have weak enrichment over background. Plots are shown on two
1464 different scales for comparison. **h**, Fraction of MAU2, OCT4, and CTCF ChIP-seq reads found
1465 in either CTCF or MAU2 peaks. OCT4 ChIP-seq is from ref[51,121].

Extended Data Figure 2

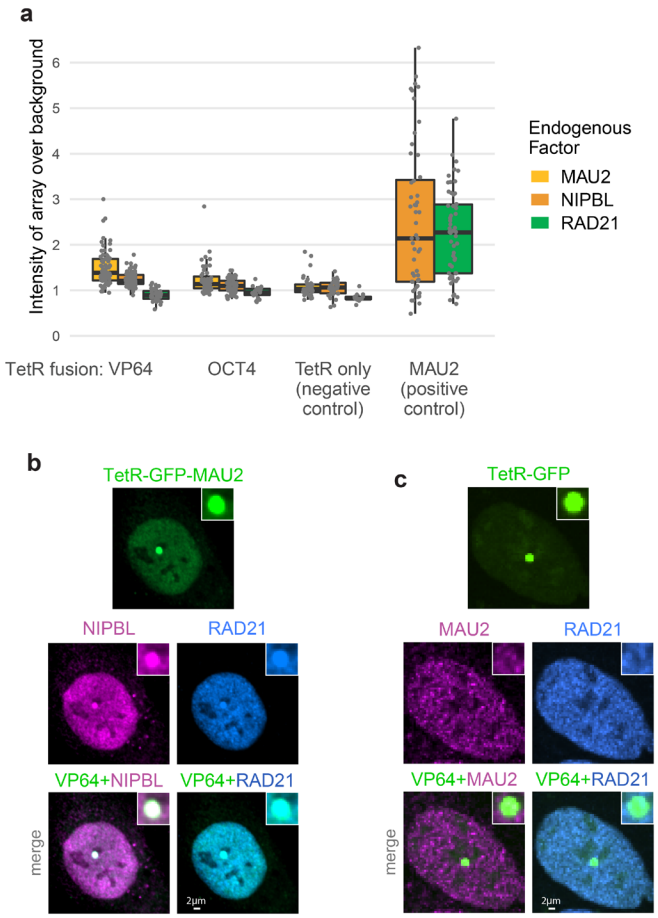

Extended Data Figure 2: Recruitment of cohesin by TetR-MAU2.
a, Intensity of MAU2, NIPBL, or RAD21 immunofluorescence signal at the TetO array divided by intensity of the background nuclear signal. **b**, Example cell showing that TetR-MAU2 recruits NIPBL and RAD21 to the TetO array. **c**, Example cell showing that TetR alone does not recruit MAU2 or RAD21 to the TetO array.

Extended Data Figure 3

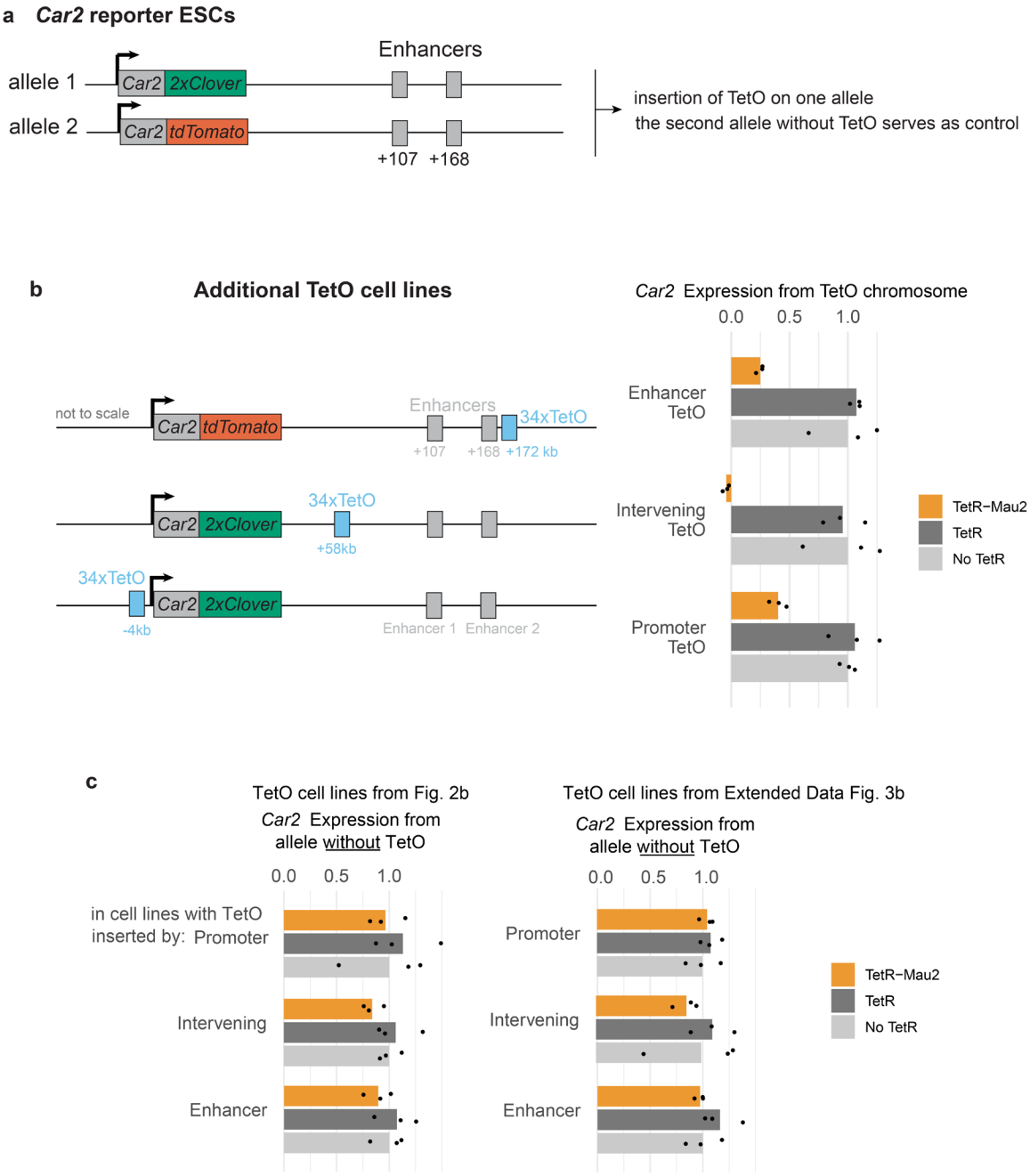

Extended Data Figure 3: Additional clones for targeted cohesin recruitment. **a**, *Car2* reporter ESCs (from ref[42]): in each cell, one *Car2* allele harbors a tdClover reporter and the second allele harbors a tdTomato reporter. *Car2* expression in cells with heterozygous TetO insertions can therefore be directly compared between the TetO allele and control allele without the TetO. **b,** Additional cell lines with TetO insertions either on the tdClover or the tdTomato allele, replicating observations reported in Fig. 2. **c**, In the same cells that displayed reduced

1479 *Car2* expression on the TetO allele upon TetR-Mau2 expression, *Car2* expression from the
1480 control allele without the TetO insertion remains unchanged across three biological replicates
1481 from separate transfections.

Extended Data Figure 4

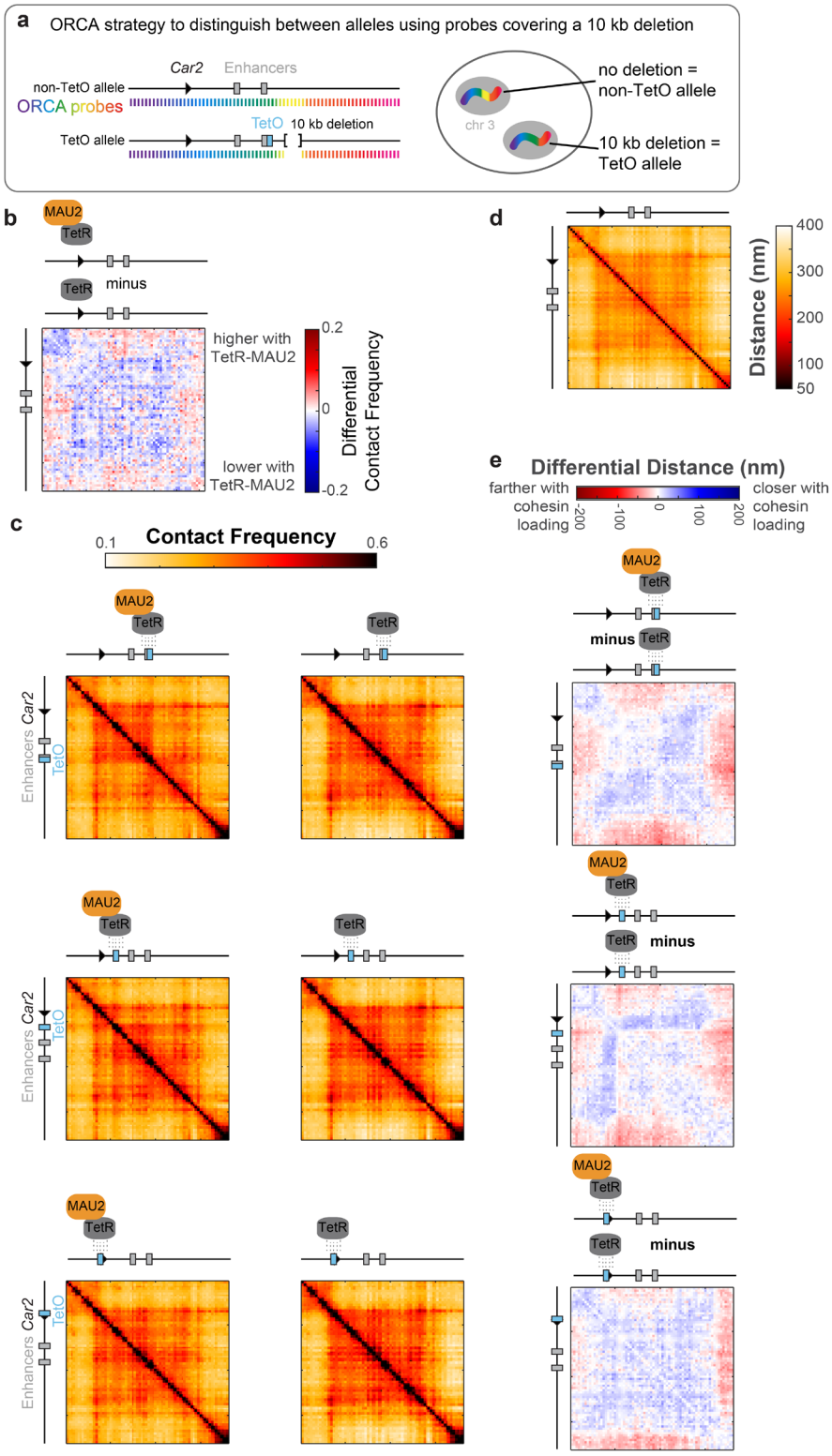

1484 **Extended Data Figure 4: ORCA measurements comparing alleles with and without high**
1485 **cohesin loading.**
1486 **a**, The TetO array used for cohesin recruitment is inserted on one allele, where we also
1487 engineered a neutral 10 kb deletion to distinguish the two alleles. This deletion enables
1488 distinguishing the two alleles, as the TetO allele will not display ORCA signal from probes
1489 covering the 10 kb deletion. **b**, ORCA interaction frequencies from the non-TetO allele are
1490 reduced upon TetR-MAU2 overexpression compared to cells expressing TetR alone. This
1491 comparison indicates that MAU2 expression slightly diminishes ORCA interaction frequencies.
1492 **c**, ORCA contact frequencies (~200 nm, see Methods) for the TetO allele in cells expressing
1493 TetR-MAU2 or TetR only (8 kb resolution). **d**, Heatmap showing the average distances at the
1494 *Car2* locus. **e**, Subtraction heatmaps comparing average distances in cells expressing TetR-
1495 MAU2 or TetR alone.

Extended Data Figure 5

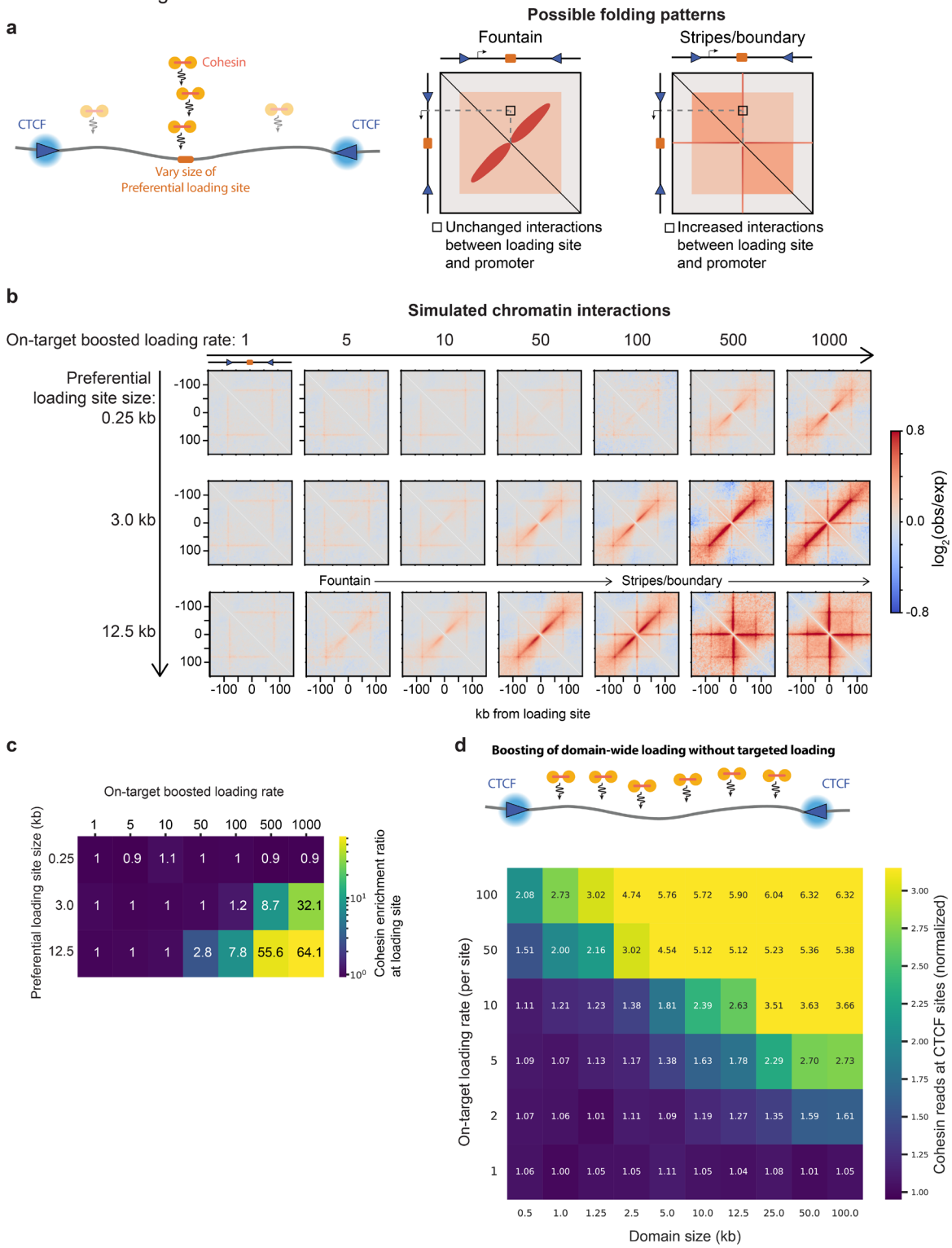

1496

Extended Data Figure 5: Width of cohesin loading site affects cohesin blocking and traffic. **a**, 3D polymer simulations in which the rate of cohesin loading is boosted at a loading site of varying size. **b**, Simulated Hi-C-like contact maps (2.5 kb resolution). Increasing cohesin loading creates fountain structures. For large loading sites with high loading, stripe patterns also emerge from the loading site, as colliding cohesin molecules block each other. **c**, 1D lattice simulations as in Figure 3A and 3B show that cohesin accumulates at loading sites only if loading is high across multiple adjacent monomers. The enrichment ratio at the loading site is calculated as the amount of cohesin in 1 kb at the center of the loading site divided by the amount of cohesin in 1 kb at a background site. **d**, Simulation exploring how boosting cohesin loading across domains of increasing size affects cohesin abundance at flanking CTCF sites.

Extended Data Figure 6

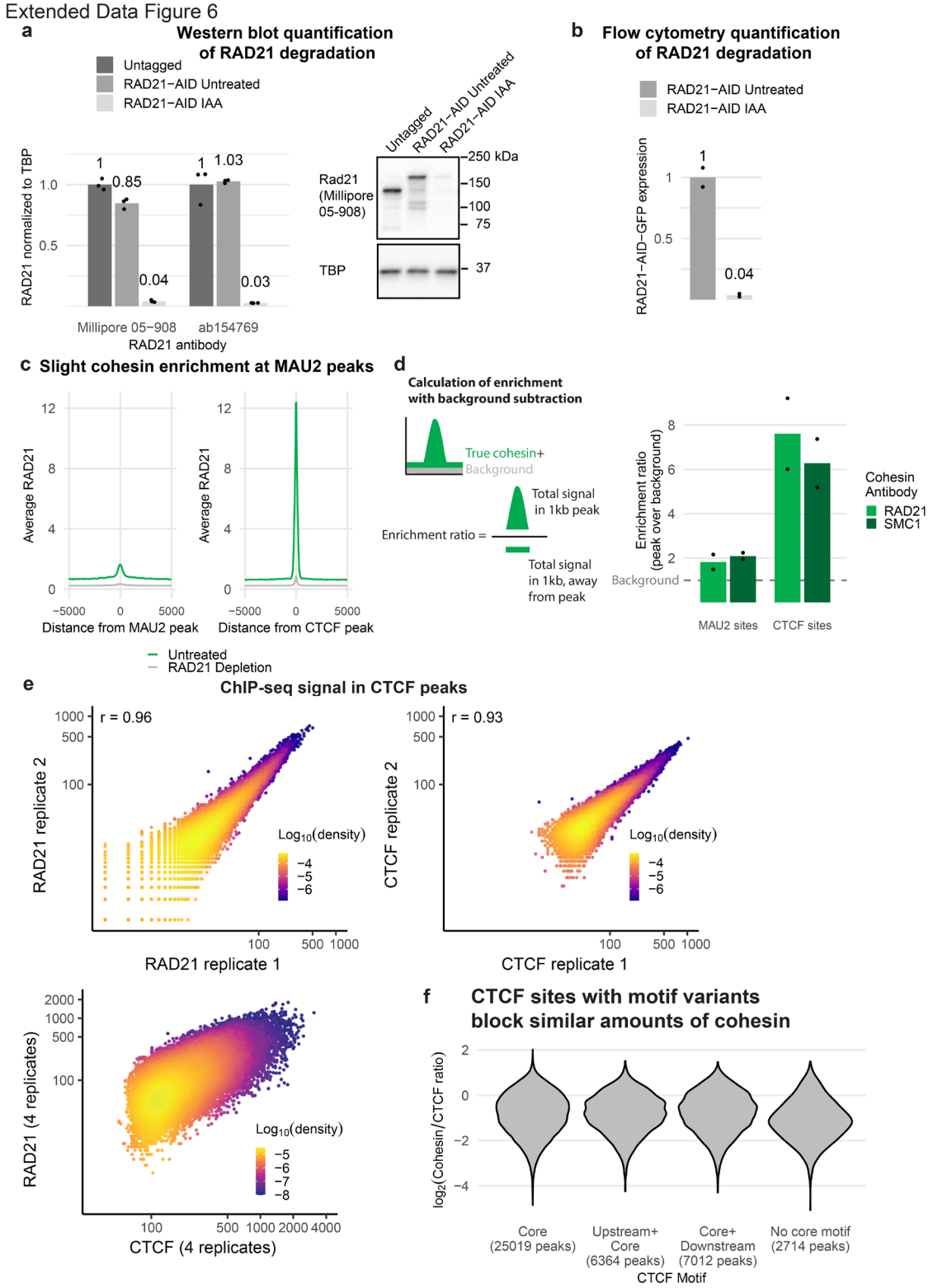

1507

1508 **Extended Data Figure 6: Cohesin is slightly enriched at MAU2 peaks, and cohesin at CTCF**
1509 **peaks is weakly correlated with CTCF occupancy.**
1510 **a**, Western blots and **b**, flow cytometry show that in RAD21-AID-GFP cells treated with IAA for
1511 3.5 hours, >95% of RAD21 was degraded. **c**, Average RAD21 signal at MAU2 peaks (that do not
1512 overlap CTCF peaks) or at CTCF peaks before or after 3.5 hr RAD21 depletion. **d**, Average
1513 enrichment of cohesin binding at MAU2 or CTCF peaks after background subtraction. **e**, At
1514 CTCF peaks, the number of reads is highly correlated between replicates of CTCF or RAD21
1515 ChIP-seq but shows wider dispersion between RAD21 and CTCF (four combined replicates
1516 reproduced from Fig. 5B for comparison). **f**, RAD21/CTCF ratios for CTCF sites based on the
1517 presence of upstream or downstream CTCF motifs[53]. Sites with upstream, downstream, or only
1518 core motifs show similar distributions, while peaks with no identifiable core CTCF motif block
1519 less cohesin.

Extended Data Figure 7

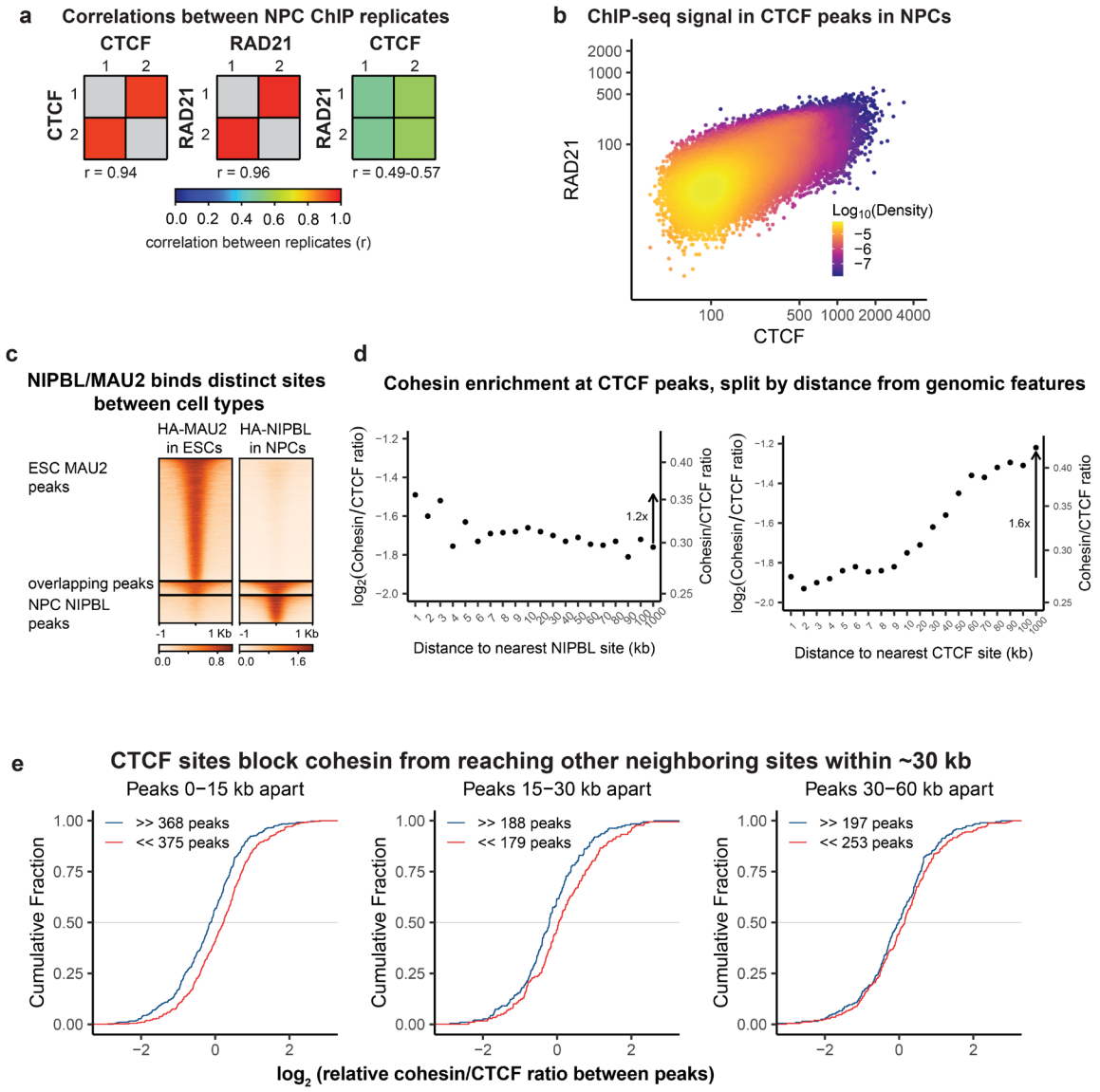

Extended Data Figure 7: CTCF sites, more than NIPBL/MAU2 sites, control cohesin traffic in Neural Progenitor Cells (NPCs) differentiated from ESCs.
a, At CTCF peaks, the number of ChIP-seq reads is more highly correlated between two CTCF replicates or two RAD21 replicates, compared to the correlation between CTCF and RAD21 (Pearson correlation coefficient). **b**, RAD21 vs. CTCF reads in each CTCF peak. Read numbers were normalized to match the number in ESCs in Fig. 5B. **c**, NIPBL/MAU2 binding sites are largely not overlapping between ESCs and NPCs. **d**, Average ratio of cohesin/CTCF reads in CTCF peaks based on the distance from the peak to the nearest NIPBL or CTCF site. **e**, The distance over which CTCF sites block cohesin in NPCs was analyzed as in Fig. 6C. Similarly to ESCs, pairs of CTCF sites with forward motifs have lower relative cohesin/CTCF ratios than pairs with reverse motifs only when the peaks are within 30 kb of each other.

Extended Data Figure 8

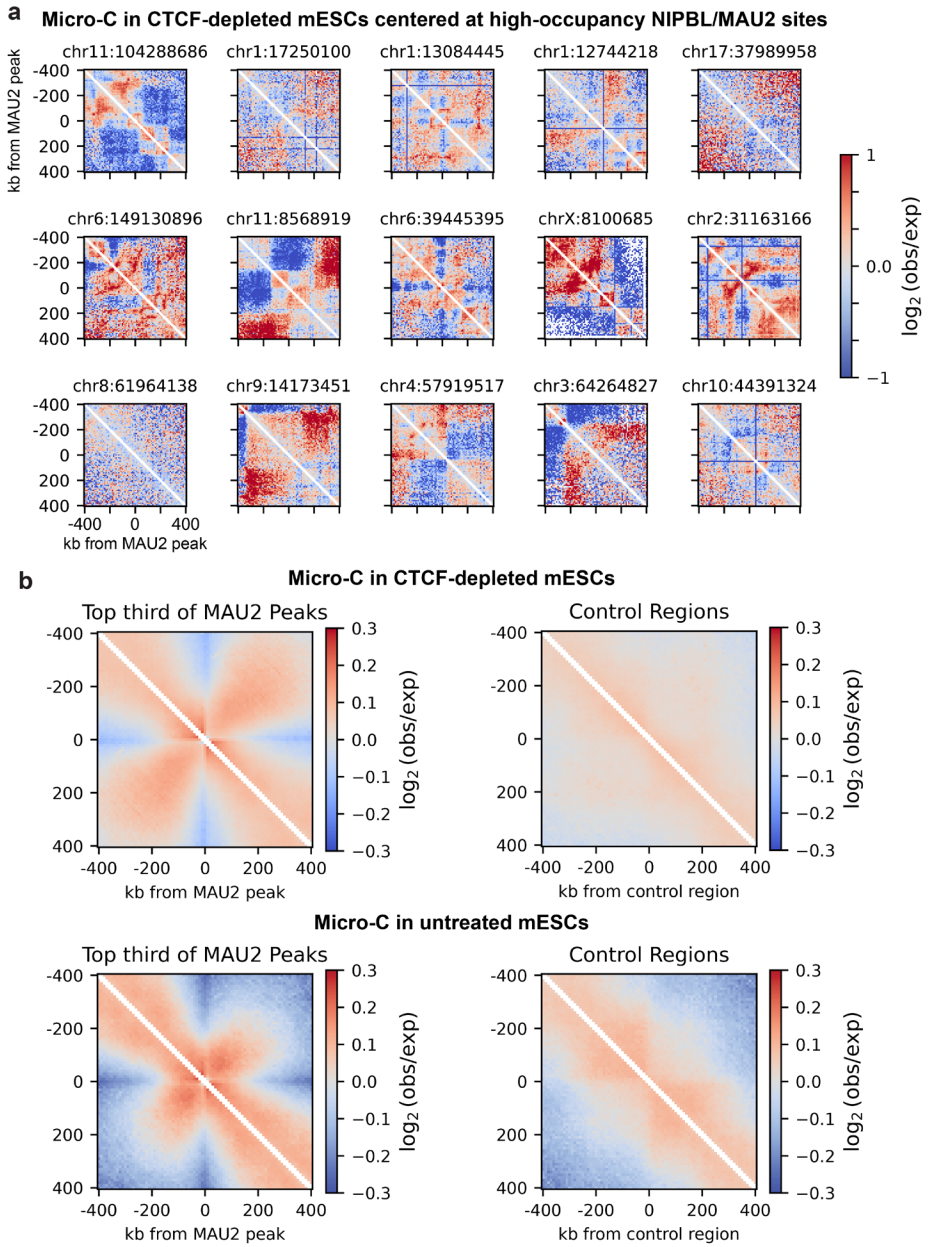

Extended Data Figure 8: NIPBL/MAU2 sites only mildly change local chromatin folding. **a**, At 15 of the highest occupancy individual MAU2 sites, micro-C in CTCF-depleted cells does not show fountain patterns. Heatmaps are plotted at 10 kb resolution. **b**, A pile-up of micro-C data in CTCF-depleted or untreated ESCs[118] at the highest-occupancy third of MAU2 sites shows a weak fountain pattern, while randomly chosen sites within the same TADs as the MAU2 sites do not.

Extended Data Figure 9

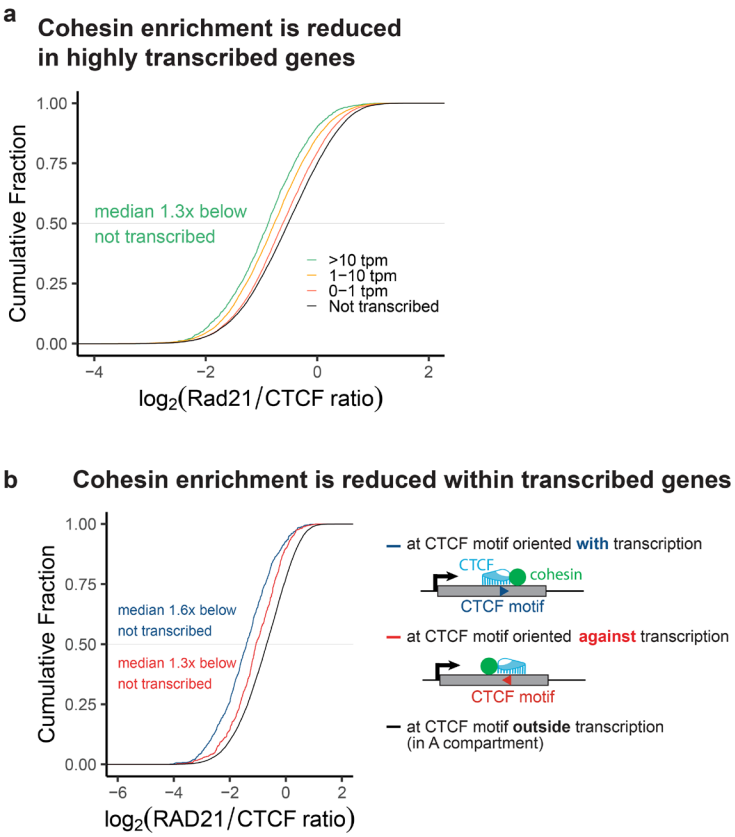

Extended Data Figure 9: Cohesin traffic is impeded in actively transcribed loci. **a**, Cumulative plot shows lower RAD21/CTCF ratios for CTCF sites within gene bodies based on their transcription level. **b**, Cohesin enrichment is reduced at CTCF sites within GENCODE protein-coding genes with RNA-seq transcription >10 tpm[115].

Extended Data Figure 10

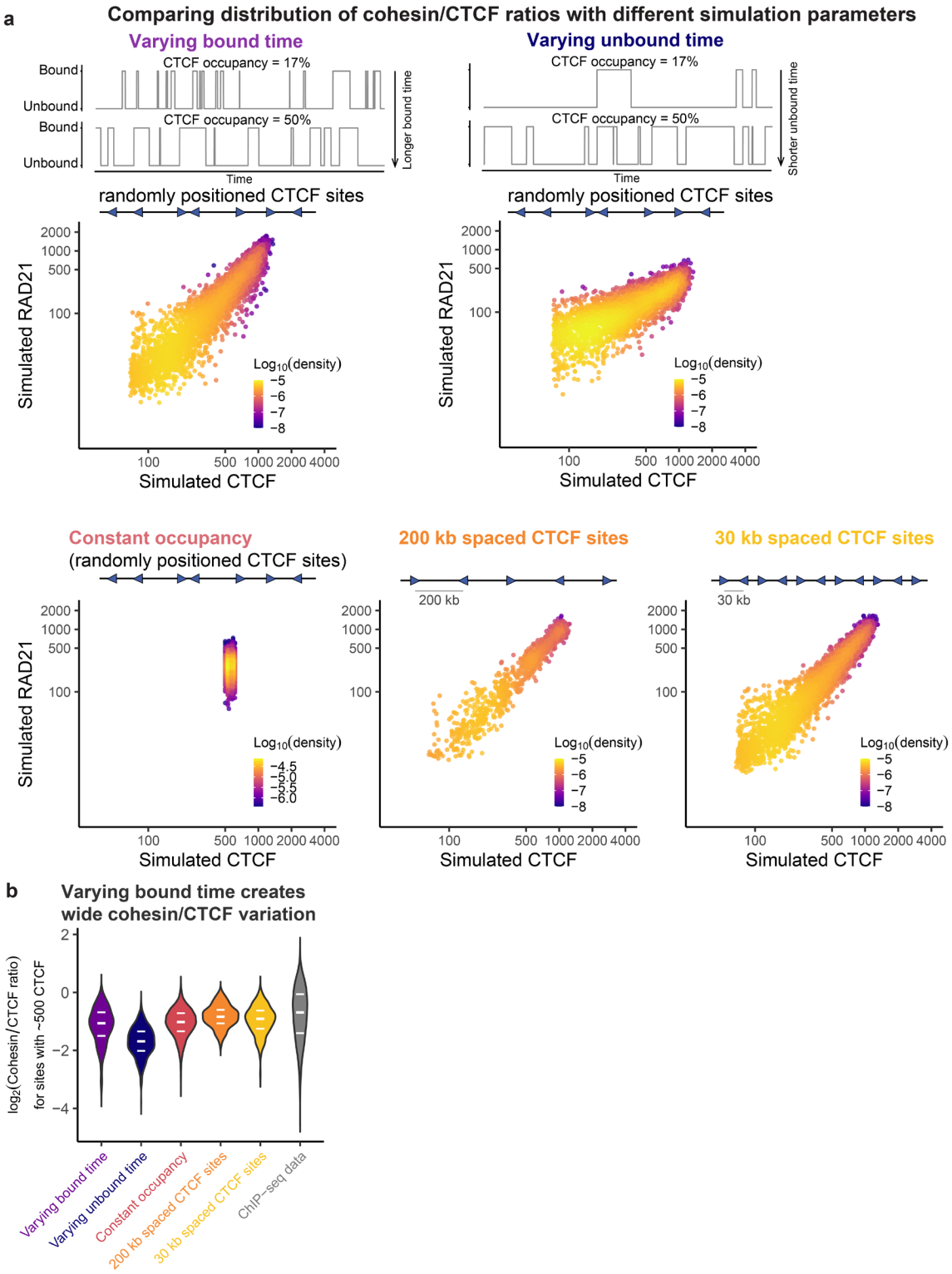

1544

1545 **Extended Data Figure 10: Comparison of CTCF/cohesin ratios using simulations with**
1546 **different parameters.**
1547 **a**, Cohesin and CTCF occupancies at CTCF sites from simulations using different parameters for
1548 CTCF site occupancy and spacing. **b**, Distributions of CTCF/cohesin ratios for each parameter
1549 compared to ChIP-seq data.

Extended Data Figure 11

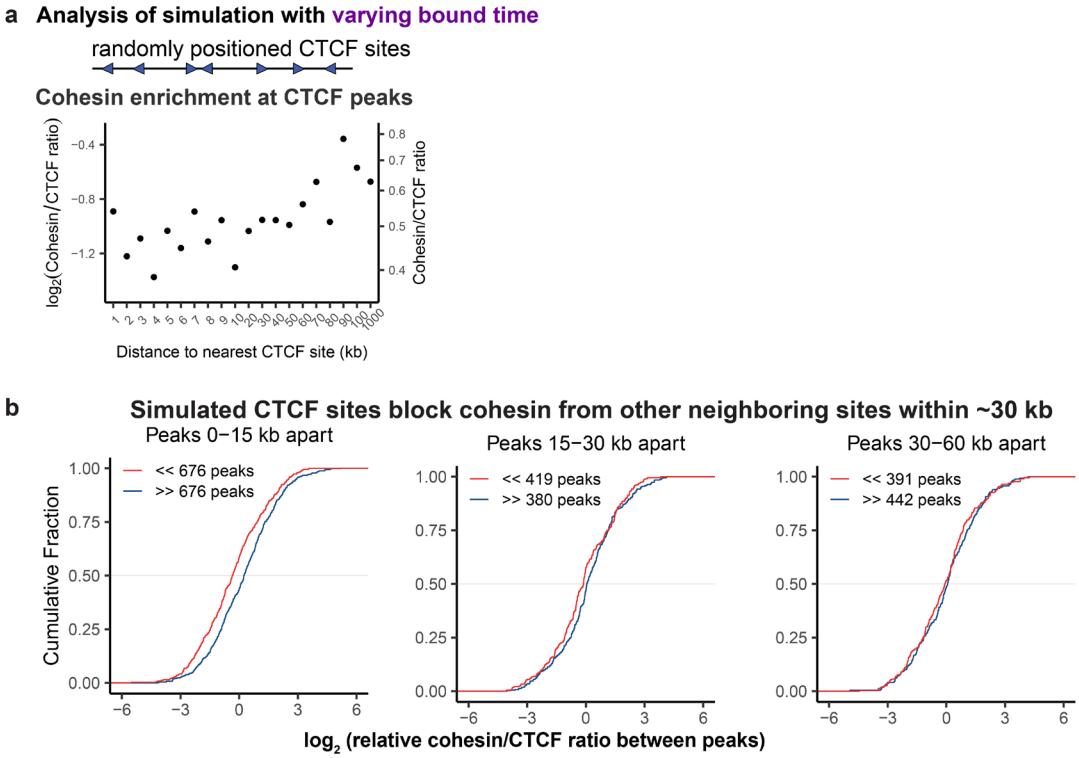

Extended Data Figure 11: In simulations, neighboring CTCF sites block cohesin traffic. **a**, Simulation quantification showing that CTCF sites near other sites have lower cohesin occupancy (compare to ChIP-seq data in Fig. 6A, Extended Data Fig. 7D). **b**, Simulation quantification showing that CTCF sites block cohesin from other CTCF sites within ~30 kb (compare to ChIP-seq data in Fig. 6C, Extended Data Fig. 7E).

Extended Data Figure 12

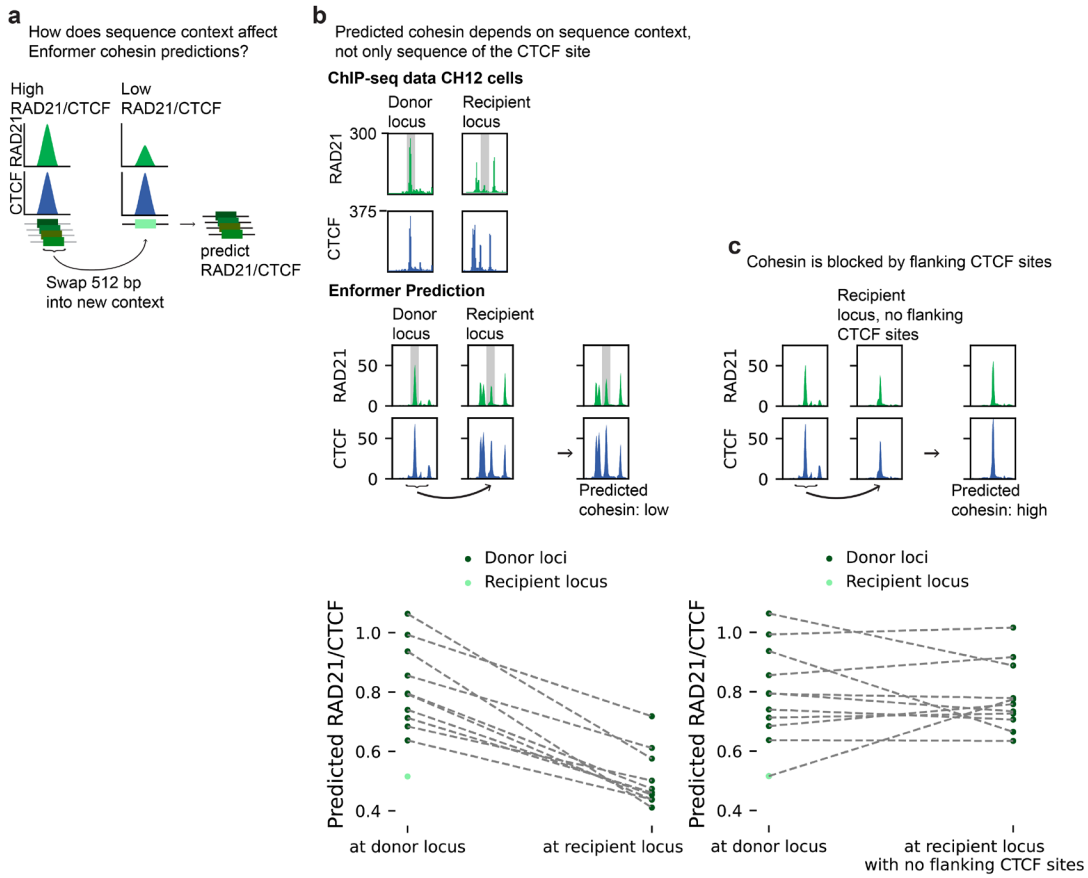

Extended Data Figure 12: Enformer predicts that clustered CTCF sites alter cohesin accumulation.
a, Using Enformer[120], we selected sites with high predicted CTCF and RAD21 levels in CH12 cells (a mouse B cell lymphoma line), swapped 512 bp from the CTCF binding site into a recipient sequence context where a high-occupancy CTCF site has low RAD21 binding, and predicted binding for the chimeric sequences. **b**, The chimeric sequences show low predicted RAD21, indicating that the sequence context affects the predicted cohesin binding. Cohesin and CTCF binding ChIP-seq data from CH12 cells[115] at the donor and recipient loci match the Enformer predictions. **c**, Without the CTCF motifs flanking the central site of the recipient locus, the predicted cohesin increased, indicating that Enformer predictions are influenced by CTCF motifs in the surrounding sequence.

Extended Data Figure 13

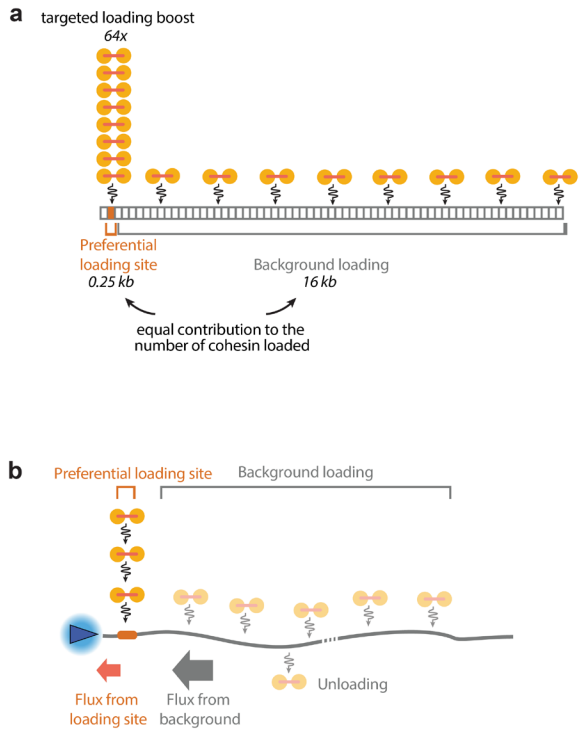

Extended Data Figure 13: Cartoons comparing the contributions of targeted versus background cohesin loading

a, As an example, with a 64-fold targeted loading boost, a 0.25 kb loading site contributes to loading as much cohesin as a 16 kb background region. **b**, Cartoon illustrating the relative contributions of targeted and background cohesin loading to the flux of cohesin reaching a CTCF site. Even when a preferential loading site exists, its contribution is easily outweighed by cohesin loaded across the surrounding chromatin at the background rate.